INAUGURAL-DISSERTATION
zur
Erlangung der Doktorwürde
der
Naturwissenschaftlich-Mathematischen
Gesamtfakultät
der
Ruprecht-Karls-Universität
Heidelberg

vorgelegt von
**Dipl.-Phys. Lars Knoll**
aus Freiburg i. Br.
Tag der mündlichen Prüfung: 21.6.2000

# Dissoziationsdynamik in der Coulomb Explosion zweiatomiger Molekülionen

Gutachter: **Prof. Dr. Dirk Schwalm**
**Prof. Dr. Jürgen Kluge**

Dissertation
submitted to the
Combined Faculties for the Natural Sciences and for Mathematics
of the Rupertus Carola University of
Heidelberg, Germany
for the degree of
Doctor of Natural Sciences

# Dissociation dynamics in Coulomb explosion imaging of diatomic molecules

presented by

Diplom-Physicist: **Lars Knoll**
born in: Freiburg i. Br.

Heidelberg, 21.6.2000

Referees: **Prof. Dr. Dirk Schwalm**
**Prof. Dr. Jürgen Kluge**

# Kurzfassung

*Dissoziationsdynamik in der Coulomb Explosion zweiatomiger Molekülionen*

Bei der Coulomb Explosion wird die folieninduzierte Dissoziation isolierter Molekülionen gemessen. Um strukturelle Parameter des Moleküls aus diesen Messungen zu extrahieren müssen Annahmen über die Form des dissoziativen Potentiales gemacht werden. Die Benutzung einfacher Coulomb Potentiale erlaubt eine sehr gute Beschreibung vieler der Messungen, erweist sich aber als zu ungenau für einen Teil der experimentell gemessenen Daten.

In dieser Arbeit werden systematische Messungen durchgeführt um ein besseres Verständnis der Dissoziationsdynamik zu erhalten. Zu diesem Zweck wurde die Coulomb Explosion von drei verschiedenen Molekülionen ($HeH^+$, $LiH^+$ und $CH^+$) gemessen. Da die strukturellen Parameter aller obigen Moleküle gut bekannt sind können sie benutzt werden um die Dissoziationspotentiale bei der Coulomb Explosion auszumessen. Die Messungen werden mit drei verschiedenen Modellen des Dissoziationsprozesses verglichen: Dem Bild einer Explosion auf Coulomb Trajektorien das eine sehr gute Beschreibung der Explosion vollständig gestrippter Ionen liefert, ein einfaches Modell, das für Explosionen bei denen ein Elektron im System verbleibt, einen Teil der Elektron-Ion Wechselwirkung mit einbezieht und einer Quantenchemischen Berechnung der Dissoziationspotentiale.

# Abstract

*Dissociation dynamics in Coulomb explosion imaging of diatomic molecules*

Coulomb explosion imaging measures the foil induced dissociation of isolated molecules. To extract structural parameters of the molecules from these measurements assumptions about the potential driving the dissociation have to be made. Using simple Coulomb potentials to model the dissociation dynamics while giving a very good description for a lot of systems does not model correctly part of the experimental data measured with Coulomb explosion imaging.

In this work systematic measurements of the dissociation dynamics happening during and after the passage of the molecular ion through the target foil are performed. Three different molecular ions ($HeH^+$, $LiH^+$ and $CH^+$) were used for this study. Since all of them are theoretically well known they can be used to experimentally probe the potentials driving the dissociation. The measurements are compared to different models describing the dissociation process: The Coulomb explosion picture which is known to work for explosions of fully stripped ions, a simple model taking into account part of the interaction when one electron remains in the system and a full quantum chemical calculation of the dissociation potentials.

# Contents

# 1. Introduction

Many years after the introduction of quantum mechanics, molecular physics is still an exciting and live field with lots of new developments and results. A large part of the interest stems from the fact that molecules and their properties play an important role in our environment. Although the laws of quantum electro dynamics which are describing the behavior of of molecules are well known there are still many unresolved questions due to the complexity of the systems which makes highly accurate ab-initio calculations of molecular properties impossible. If trying to determine molecular properties from first principles, computational chemistry reaches its limits already at 3–5 atomic molecules. For dynamic behavior, even two atoms can already be too much. Due to this complexity even small and isolated molecules exhibit a rich set of properties that are interesting to study. Most of the experimental knowledge about isolated molecules comes from measuring the electromagnetic spectra of these species [1]. Structural parameters can be extracted by assigning these lines measured spectroscopically to rotational and vibrational transitions using model potentials and comparing to ab-initio calculations. These structural properties can then serve as a starting point for the study of dynamic properties such as molecular collisions and chemical reactions.

A different approach to obtain information about the structure of isolated molecules is by induced dissociation of the molecule. Assuming that one knows the laws driving the dissociation it is possible to extract information about structural data of the molecules prior to its dissociation from the measurement of the dissociation products. This method is used by the *Coulomb explosion imaging* technique (CEI) [2] presented in this work which is based on the foil induced dissociation of fast molecular ions. Most of the electrons inside the molecule get scattered away as the molecule passes the foil and the resulting positively charged ions start to explode due to the Coulomb repulsion acting between them. Assuming a simple Coulomb potential between the fragments information about the initial spatial structure of the molecule when entering the foil can be extracted from the measured asymptotic velocities of all the ionic fragments emerging from the foil. Since the dissociation is fast compared to the time-scales of molecular motion a "snapshot" of the molecule at the moment it enters the foil is obtained. Measuring many molecules results in a distribution in velocity space that can be related to the spatial structure of the molecule in configuration space before the explosion. As it is difficult to accelerate neutral molecules this method is usually used for charged molecular ions (see for example [3]). Because of their high reactivity molecular ions are not easily investigated experimentally and make Coulomb explosion imaging an interesting possibility to reach a better understanding of molecular ions. Molecular ions are especially important in low temperature plasmas as found for example in interstellar clouds and as intermediate products of chemical reactions. CEI has also been applied to the measurement of neutral molecules by accelerating negative molecular ions and then photo-detaching them before the measurement [4]. As the CEI technique directly measures structural parameters of the molecule it is especially suited to measure so called “floppy” molecules (molecules showing large amplitude motions in some internal degree of freedom) for which the interpretation of spectroscopical data is especially difficult.

A few other methods to initiate the dissociation of the molecule exist, namely using femtosecond laser pulses [5], by photons from a synchrotron radiation source [6] and by ion impact [7]. Obtaining structural parameters of molecules from these measurements is however not always possible. Interactions with femtosecond laser pulses are usually not fast enough compared to vibrational time scales of the molecule. Dissociation by ion impact often has the problem to produce low charge states of the dissociating fragments which makes it difficult to extract informations about the molecules initial structure because the explosion does not happen on Coulomb potentials [7]. Although in CEI the average measured charges are higher than obtained by ion impact ionisation the difficulty of extracting information from the dissociation into low charge states is something that also happens in CEI and will be one focus in this work.

To be able to compare theoretical calculations to experimental data in Coulomb explosion the rovibrational and electronic states the projectile molecules occupy have to be known. In older CEI experiments this was done by using molecular ion sources build especially to produce internally cold molecular ions [8]. As no independent method to measure the internal excitations existed and it was rather hard to control the exact conditions of the source and comparisons to theory were rather difficult to do. A different way to produce internally cold molecular ions is to store them after their production for a time long enough for them to relax to thermal equilibrium with their surroundings. For molecular ions with a velocity of a few percent the speed of light a storage ring such as the TSR at the Max-Planck-Institut für Kernphysik in Heidelberg [9] is an ideal device to store them for a few seconds. This storage time is long enough for most molecules to relax vibrationally. The ability of the TSR to prepare internally cold, fast molecular ions has been used in a number of experiments studying dissociative recombination (see e.g. [10, 11]) and photo-dissociation [55]. In one of the first CEI experiments at the TSR the cooling of vibrationally excited molecules could be observed directly [12] and used to measure the dissociative recombination cross sections of higher excited vibrational states of $HD^+$. All this makes the storage ring an ideal tool to be able to measure Coulomb explosion imaging of molecular ions during and after their vibrational deexcitation. The whole experiment has been build up in close collaboration with the Weizmann Institute of Science in Rehovot, Israel [13]. Several molecular ions have been investigated with the CEI setup at the TSR. These investigations showed that for some cases the theoretical description of the dissociation process by a pure Coulomb interaction between the fragments is insufficient to describe all the features seen in the experimental data [14]. These problems occured mainly for channels where the molecule dissociated into lowly charged fragments. To examine these effects a series of measurements of the molecular ions $HeH^+$, $LiH^+$ and $CH^+$ were performed and will be described in this thesis. These ions are the simplest molecules where one can expect deviations from the simple model of an explosion on Coulomb trajectories. This model is known to work well for the explosion of fully stripped ions as has already been seen in the measurement of the simplest molecular ion $HD^+$ [14]. All the above molecules are theoretically well understood and both $HeH^+$ and $CH^+$ were already stored and used for other measurements in the TSR. Although the molecules are all build up from a hydrogen and one heavier atom they are quite different concerning their internal structure thus covering a wide range of initial configurations. Using the known structure of the molecules the processes happening during the dissociation can be probed. One can now hope to find out if there are other conditions where the approximation of an explosion on Coulomb trajectories is valid and try to find effective descriptions for the cases where this model fails to describe the processes happening during the dissociation.

The following chapter will introduce the Coulomb explosion imaging method and discuss the current methods used to correlate experimental data to theoretical calculations. The successes and shortcomings of this approach will be discussed. In the third chapter the known properties of the measured molecules $HeH^+$, $LiH^+$ and $CH^+$ as far as they are relevant for this thesis will be reviewed and chapter four explains the experimental setup of the CEI experiment at the storage ring TSR. Chapter five will show and discuss the measurements of the three molecular ions and compare them to theoretical expectations.

# 2. Coulomb Explosion Imaging

Coulomb explosion imaging (CEI) was introduced in the late seventies [15] as a method to measure molecular structures. It is based on the study of the foil induced dissociation of fast molecules. Technical improvements have allowed the detailed measurement of complex molecules since 1989 [2]. The structures of many systems composed of between two [16] and five [17, 18] atoms have since then been investigated using the CEI technique.

A new experimental setup that merges the Coulomb explosion imaging technique with a storage ring has been recently constructed at the heavy ion storage ring TSR [13]. The advantages of merging the CEI experiment with the storage ring facility in Heidelberg will be discussed in the next chapter. The molecular species measured in Heidelberg so far include $HD^+$ [12, 19], $CH_2^+$ [3], $NH_2^+$, $DCO^+$and its isomer $DOC^+$ [14] as well as $H_3^+$ [20]. This work will analyze the molecular ions $HeH^+$, $LiH^+$ and $CH^+$.

## 2.1 Principles of CEI

When a molecular ion enters a solid target with a velocity of a few atomic units[1], the electrons that account for the binding of the molecule are scattered away in the first few atomic layers leading to the dissociation of the molecule [21, 22, 23]. The cross section for this process can be estimated by simple geometrical arguments to be of the order of $\sigma = 10^{-16}\,\mathrm{cm}^2$. Molecules with a velocity of e. g. four atomic units therefore loose their binding electrons in the target (which typically has a density of about $n_{\mathrm{Target}} \approx 10^{23}\,\mathrm{cm}^{-3}$) within a time of

$$\tau = \frac{1}{\sigma n_{\mathrm{Target}} v_{\mathrm{mol}}} \approx 10^{-16}\,\mathrm{s} \quad . \tag{2.1}$$

This corresponds to a distance of $\mathrm{d} = v_{\mathrm{mol}} \cdot \tau$ of approximately 10 Å, so the stripping takes place in the first few atomic layers of the target. This is much faster than any time scale on which processes inside the molecule (vibrations and rotations) happen. The fastest molecular

---

[1] 1 atomic unit or 1 a.u. corresponds to 27.211 eV, a velocity of $\alpha c$ or 1/137 the speed of light and a distance of 0.529 Å.

processes are stretching vibrations which usually happen on a time scale of about $10^{-14}$ s. Rotations are about two orders of magnitude slower.

Thus in a time scale in which one can assume the nuclei of the molecule to stay fixed the molecular potential which binds the molecule is transformed to a dissociative potential due to the Coulomb repulsion between the nuclei, leading to an explosion of the molecule. If the foil is thin enough ($\lesssim$ 100 Å) the molecule leaves the foil in less than $10^{-15}$ s and most of the explosion takes place in the vacuum after the foil until the fragments reach their asymptotic velocities. After about $10^{-13}$ s most of the initial potential energy between the fragments is converted into kinetic energy. After a few meters of flight when the fragments have a relative distance of a few centimeters they are detected on a position and time sensitive detector. The whole process is shown schematically in figure 2.1.

During the passage through the foil the charge states of the atomic fragments can change due to stripping and electron capture [24]. So the potential inside the target changes with the charge state of the fragments. It is also partly screened due to the electrons of the target. Additional effects happening in the target are multiple small angle scatterings, which is, besides the Coulomb explosion, the main process determining the final velocities of the fragments [24, 25, 26]. If the target is made from a low Z material, collisions leading to large scattering angles are rare. Energy loss of the ion in the target can be neglected for single ions in such thin targets. For molecules, however, the wake field produced by one ion can influence the

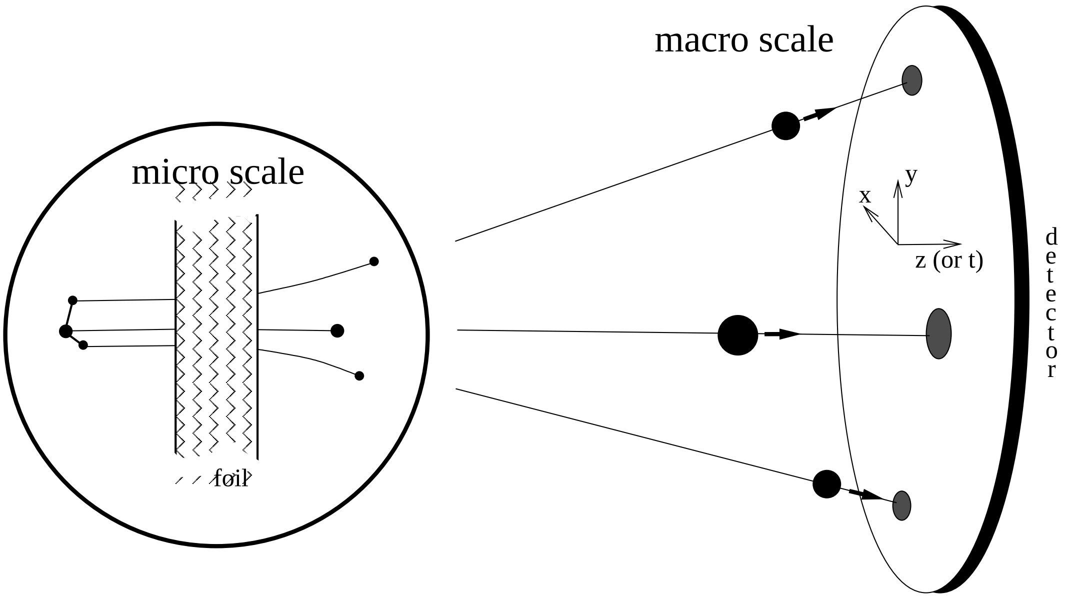

**Fig. 2.1:** *The principle of CEI. A very fast molecular ion hits a thin foil. The valence electrons get stripped off, and an explosion begins due to the Coulomb repulsion of the fragments. These get detected on a time and position sensitive detector.*

other fragments and lead to a change in the relative velocities between the fragments. This is noticeable especially if a light particle travels in the wake field of a highly charged ion. In this case the wake field can change the measured velocity distribution even though the energy loss in the target is negligible [27, 28].

By measuring the time at which each particle hits the detector and its position one can calculate the asymptotic velocities of all fragments of the dissociating molecule by using the geometry of the detector. This measured set of final velocity vectors $\mathbf{V}_i$ $(i = 1 \ldots N)$ of all $N$ fragments of the molecule contains information about its structure at the moment the molecule hits the foil, giving rise to the name of the technique: Coulomb explosion imaging [2, 29]. By measuring many of these events, one obtains a distribution of the asymptotic fragment velocities $\mathrm{P}(\mathbf{V}_i;\ i = 1 \ldots N)$, the so called "$V$-space distribution". This distribution then reflects the distribution of molecular configurations in real space which for a molecule in a single state corresponds to the square of the nuclear wave function. The $V$-space distribution is usually calculated in the center of mass frame of the dissociating molecule, but other conventions can be used where needed. Since the beam velocity $\mathbf{v}_{beam}$ is non relativistic, the transformation between laboratory frame and center of mass frame is given by

$$\mathbf{V}_{i,Lab} = \mathbf{V}_{i,cm} + \mathbf{v}_{beam} \tag{2.2}$$

If the target effects are small and a good detector resolution is achieved the asymptotic velocities measured on the detector depend mainly on the initial configuration in the configuration space of the molecule (here often referred to as "$R$-space distribution"), when the molecule entered the target. As long as the Coulomb potential energy (which is typically of the order of $10 - 100\,\mathrm{eV}$) is large compared to the kinetic energy stored in the molecular wave function, this kinetic energy can be neglected. Contributions from multiple scattering are small due to the extremely thin target foils used. The distribution of measured relative velocities gets smeared by a few percent at most due to these effects for the molecules measured in this thesis. The contribution due to wake fields depends on the orientation of the molecule when it enters the target foil, and its influence can be minimized by applying a cut on the measured $V$-space distribution as described in section 4.6. The main foil effects, multiple scattering and charge exchange can be described theoretically and are therefore taken into account when comparing experimental data to calculations (see section 2.3),

To a first approximation the ions leave the foil in certain charge states $Q_i(i = 1 \ldots N)$. In the vacuum behind the foil they then explode along Coulomb trajectories. Experiments with molecular ions which get completely stripped inside the foil, showed that this approach is valid and works very well if one can describe the ions leaving the foil as a group of independent, point-like particles (see also section 2.5). For most molecular ions deviations from this picture have to be taken into account. Some electrons of the molecule get stripped off inside the foil while others remain. In this case, one has a set of dissociative potential surfaces which the dissociating molecule can go into, and which govern the dynamics of the explosion. Thus a molecule like $CH^+$ for example is transformed inside the foil into an unstable $CH^{3+}$ molecular ion. The spatial structure and the wave function of the nuclei still has not changed by this time (if the foil is thin enough) as the stripping of the electrons happens much faster than any nuclear motion in the molecule. But now the nuclear wave function is not located in the bound potential of the $CH^+$ anymore but is instead populating the dissociating potential curves of the $CH^{3+}$ system. In principle one therefore has to take into account all dissociative potentials and the transition probability into each of these and calculate the explosion along these potentials to obtain the final $V$-space distribution as measured on the detector from the initial structure of the molecule.

The above approach however is too complicated to realize it for complicated molecules. It is thus important to investigate how far the simpler approach of an explosion of point-like particles holds. It is clearly valid for molecules where all electrons get stripped off. The same might be true for a dissociation of $CH^+$ into $C^{4+}$ and $H^+$. The two remaining electrons are so deeply bound in the carbons s-shell that they rarely get excited in the foil. The extension of their wave function is far smaller than the initial bond length between the carbon and the hydrogen. In this sense, one can speak also here of the interaction of two point-like particles, and the simple Coulomb model should hold.

## 2.2 Comparing experimental data to theory

For a diatomic molecule, the connection between $R$-space and $V$-space is straightforward if one neglects foil effects. Assume we have an initial distribution of intra molecular distances $P(R)$. After the foil one has two fragments at distance r, with charges $Q_1$ and $Q_2$ which repel each other due to the Coulomb forces acting between them. In the center of mass frame, with $\mu$ being the reduced mass and $v(t)$ the velocity between the fragments energy conservation does then give:

$$E_{total} = \frac{Q_1Q_2}{R} = \frac{Q_1Q_2}{r(t)} + \frac{1}{2}\mu v(t)^2 \tag{2.3}$$

Integrating over the velocity $v(r(t))$ gives

$$t(r) = \int_R^{r(t)} \frac{1}{v(r')}\mathrm{d}r' = t_{\mathrm{Coul}} f(r/R) \quad , \tag{2.4}$$

where the function $f(x)$ is given by

$$f(x) = \int_1^x \sqrt{\frac{x'}{x'-1}}\mathrm{d}x' = \sqrt{x(x-1)} + \ln(\sqrt{x} + \sqrt{x-1}) \quad . \tag{2.5}$$

The characteristic Coulomb time, after which the bond length has increased by 23% is given by

$$t_{\mathrm{Coul}} = \sqrt{\frac{\mu R^3}{2Q_1Q_2}} = 1.9\ \mathrm{fs} \times \sqrt{\frac{\mu[\mathrm{a.m.u}](R[\text{Å}])^3}{Q_1Q_2}} \quad . \tag{2.6}$$

From this one can calculate that after about $10^{-13}$ s (corresponding to about $0.1\,\mu$m flight distance) 99% of the initial Coulomb energy has been transformed to kinetic energy.
The final velocity V $= \lim_{t\to\infty} v(t)$ can be calculated directly form equation 2.3 to be

$$V(R) = \sqrt{\frac{2Q_1Q_2}{\mu R}} = 0.023\ \mathrm{a.u.} \times \sqrt{\frac{Q_1Q_2}{\mu[\mathrm{a.m.u.}]R[\text{Å}]}} \tag{2.7}$$

With $|P(V)dV| = |P(R)dR|$ one gets the transformation formula between real space and ve-

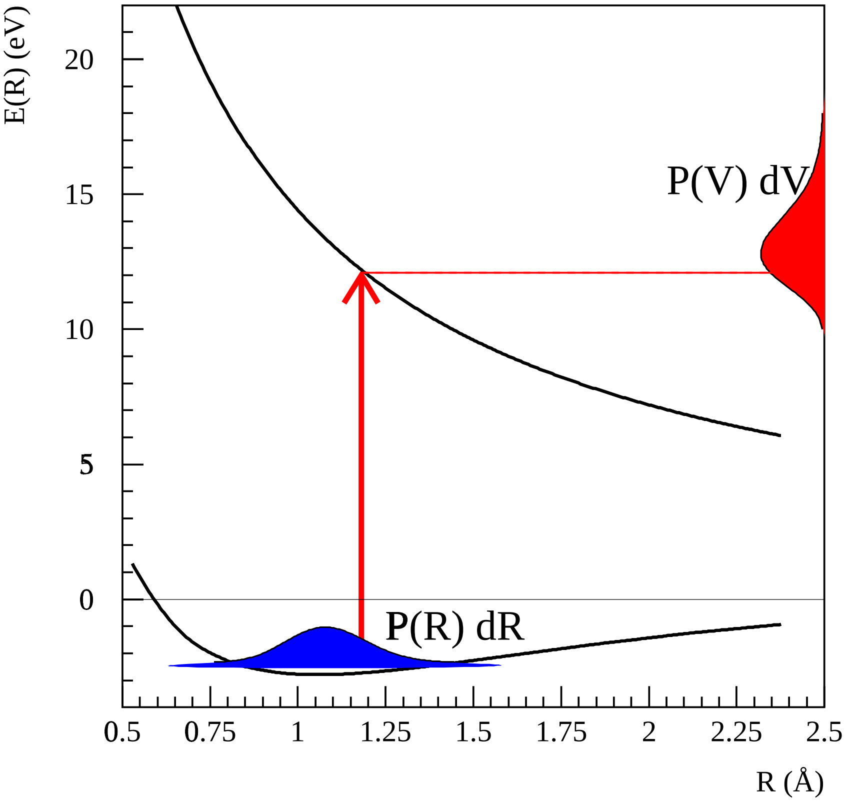

**Fig. 2.2:** *Schematic view of the Coulomb explosion of a diatomic molecule. The initial density distribution P(R) undergoes a vertical transition onto a dissociative potential curve and is projected onto a distribution P(V) in velocity space.*

locity space as follows:

$$P(V) = \sqrt{\frac{Q_1 Q_2}{2\mu}} R^{-3/2} \times P(R) \tag{2.8}$$

This is shown schematically in figure 2.2. It is thus easily possible to calculate the density in real space from the measured $V$-space distribution assuming smearing effects from the foil and detector can be neglected. From eq. 2.7 one can also see that typical final velocities between the fragments are of the order of a few percent of an atomic unit.

For molecules with more than two atoms or when one has to take influences of the target effects into account, the transformation from $R$-space to $V$-space can only be calculated numerically. For this purpose a Monte-Carlo simulation has been developed [24, 25] which will be explained in detail in the next section.

## 2.3 Simulation of the Coulomb explosion process

A Monte Carlo simulation is used to transform an arbitrary $R$-space distribution into a corresponding $V$-space distribution. The input needed for this distribution is the type of molecular ion (number and type of atoms), the velocity of the ion, the target thickness and its properties. As a classical trajectory calculation the simulation cannot calculate the propagation of a wave function but uses a number of initial configurations (events) sampled from the assumed initial $R$-space distribution. The calculation is performed in the laboratory frame. The transformation of the resulting $V$-space distribution into the center of mass frame of the dissociating molecule is straightforward. Multiple scattering, charge exchange processes and shielding is included in the simulation whereas wake effects and energy loss are not taken into account.

A schematic view of the simulation process for one event is shown in figure 2.3. If the molecule is build up of N atoms the simulation processes will generate a list of scattering events $(\mathrm{n}, \Theta, \Psi)_i$ for the atoms (n = 1...N). $\Theta$ describes the angle of the scattering, and $\Psi$ its direction. $\Psi$ is evenly distributed between 0 and $2\pi$. The scattering angle $\Theta$ is calculated according to the binary collision model described in [30]. See also [24] for a more detailed description.

The distance of travel between successive collisions is computed independently for each ion by a Monte Carlo method. If one assumes a cross section $\sigma_0$ for a scattering between the ion and an atom in the target and a random distribution of atoms in the target the scattering probability as a function of the distance of travel $d$ in the target is given by

$$p = 1 - \exp\left(-n\sigma_0 d\right) \quad . \tag{2.9}$$

The simulation starts by putting the molecule at the entrance of the foil and rotating it randomly in space. During the simulation each ion has a charge state between 0 and the nuclear charge of that ion. The initial charge state of all ions forming the molecule is usually set to zero. The simulation then integrates the equations of motion up to the point where an ion gets scattered. The interaction potential between the fragments of the molecule is assumed to be of the form of a screened Coulomb interaction using the current charge states of the ions. Then the trajectory of the scattered ion gets changed according to the scattering angle computed beforehand and the ion might loose or gain an additional electron.

The cross section for electron loss is assumed to be equal to the sum of the geometrical cross sections of the electrons bound to the ion. For an electron in the shell $n$ the geometrical cross section is given by

$$\sigma = \pi r_n^2 = \left( \frac{n^2}{Z - N_n} \right)^2 \tag{2.10}$$

where $N_n$ is the number of electrons in shells $n'$ with $n' < n$. The capture cross section for the ion is computed using the equilibrium charge state distributions given by [31] and detailed

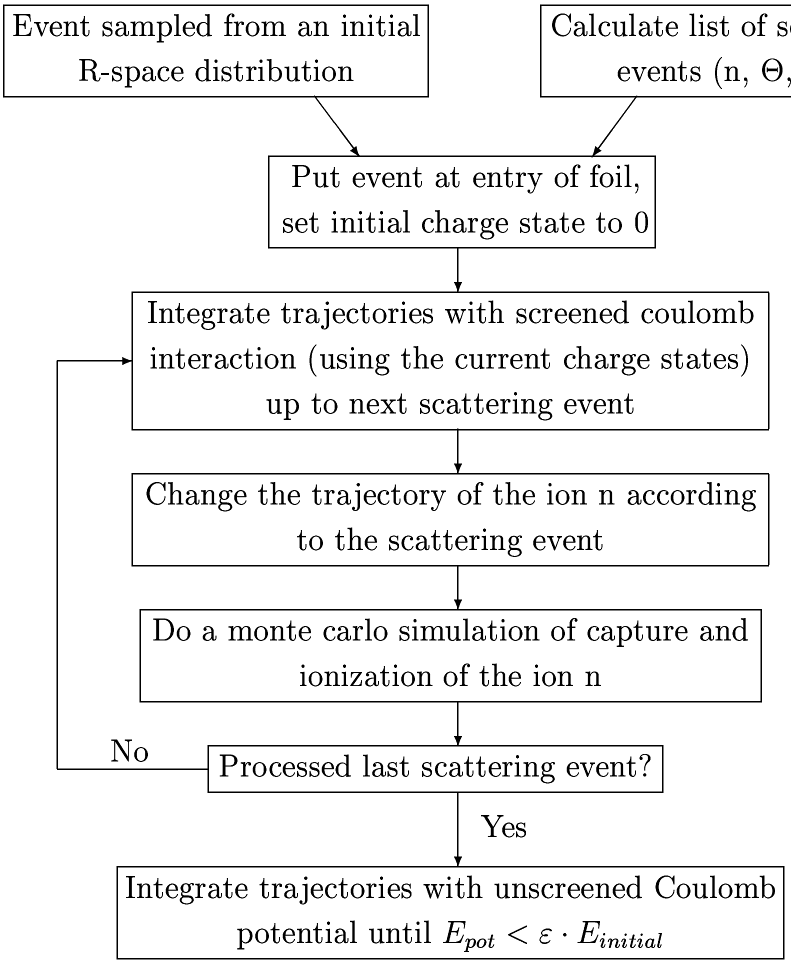

**Fig. 2.3:** *Diagram of the Monte Carlo Simulation of the CEI process*

balance with the loss cross section. This ensures that for very thick targets the simulated charge state distribution will converge to the equilibrium distribution.

The last steps are repeated until the last scattering event is processed which is at the point where the fragments leave the foil. From there on the trajectories of the fragments are calculated assuming a Coulomb like interaction (without screening) and the charge states of the fragments after the last scattering. The integration is stopped when the potential energy remaining in the system dropped below a certain percentage $\varepsilon$ of the initial potential energy when the explosion started.

After having obtained the final velocities for the event the influence of the detector is simulated in a second step. To do so another trajectory calculation is used which models the detector taking into account the magnetic field in the charge-separating magnet after the target (see section 4.2) and the finite resolutions of the detector. This finally results in a simulated data point in the same coordinates as measured during a CEI experiment. Using typically $10^5$ trajectories with $R$-space configurations sampled from the assumed density distribution of the molecule then gives a set of events that can directly be compared to experimental data.

To be able to extract a $R$-space density from a measured $V$-space distribution one has to invert the transformation given by the Monte Carlo simulation. This can be done in an iterative way where one expands the assumed initial $R$-space distribution into a set of orthogonal functions with variable coefficients. This trial distribution is then transformed into $V$-space with the help of the Monte Carlo simulation explained above and the deviations of the obtained $V$-space distribution from the measured one is used to correct the coefficients for the trial distribution in $R$-space. The process is then repeated with the corrected $R$-space density. A more detailed explanation of the algorithm can be found in [32, 14].

## 2.4 Review of the current simulation

The Monte-Carlo simulation to reconstruct the molecular structure from the measured $V$-space distribution can only work if the assumptions used in the modeling of the CEI process are valid. This section will try to give a critical review of the CEI model described above. The most important assumptions and approximations used in the model of the CEI process are as follows:

- simulation of the multiple scattering in the foil
- simulation of the charge exchange processes in the foil
- screening effects in the foil

- neglection of wake effects
- explosion happening on Coulomb trajectories and the assumption of point-like ions
- simulation of the explosion is described purely classical, no quantum mechanical effects are taken into consideration

Multiple scattering has been studied in lots of experiments and the formulas available are known to describe small angle scattering very well [24]. Almost the same is true for charge exchange processes inside the foil. Comparisons of our simulation to experimental measurements of atomic beams passing through foils of different thicknesses show a good agreement as well in the scattering as in the distribution of the final charge states [24]. It is quite hard to estimate if screening effects in the foil are taken into account correctly but with the thickness of the foils we have nowadays, over 98% of the explosion takes place after leaving the foil so a small change in the screened potential inside the foil hardly affects the simulated $V$-space distribution. Wake effects are completely neglected in the current simulation but seen in the experimental data. They occur when one ion flies through the wake created by another ion. So two of the ions have to fly through the foil on more or less the same path one after the other. Because of that this effect only occurs for certain orientations of the molecule before it hits the foil and such events can be easily cut out of the measured data.

So these four points are either understood quite well, do not affect the measured $V$-space distribution, or can be cut out of the measured data and can thus be dealt with. More critical are the last two points in the list above.

The assumption that the ions are point-like does only hold when the remaining electrons are so deeply bound that the extension of their wave functions is much smaller than the bond length of the molecule. For hydrogen-like wave functions the expectation value $\langle r \rangle$ of the distance $r$ between nuclei and electron is given by (in atomic units)

$$\langle r \rangle = \frac{1}{2Z}\Big(3n^2 - l(l+1)\Big) \quad . \tag{2.11}$$

A few of these expectation values for different ions are shown in table 2.1. Typical bond length of molecules are of the order of 2 atomic units so one can see that electrons sitting in the ground (1s) state of the ion should not influence the Coulomb explosion picture too much since the wave function does not extend into the region, where the explosion happens. If, on the other hand an electron is in a higher excited state things start to get more difficult. The other ion is then still in the electron cloud of the first one, so the potential is not point-like anymore and as a second point this ion will also influence the binding of the electron to the first ion. The correct way to calculate this is to use the full molecular Hamiltonian in the Born Oppenheimer

| Ion | He (1s) | He (2s) | C (1s) | C (2s) | C (3s) |
|---|---|---|---|---|---|
| $\langle r\rangle$ | 3/4 | 3 | 1/4 | 1 | 27/12 |

**Tab. 2.1:** *Expectation values for an electron sitting in a hydrogen state of a specific ion. Distances are in atomic units.*

approximation to be able to calculate a set of potential surfaces and use these for the explosion dynamics. Since this is usually computationally too expensive one can try to assign the electron to one of the ions and use atomic wave functions instead. This approach will be studied later on in this work and will be compared to calculations which take the full molecular Hamiltonian into account.

The last critical point is the purely classical description of the Coulomb explosion process. There are two cases where this description may fail. The first one is the case when the kinetic energy contained in the initial wave function is not small compared to the kinetic energy release in the explosion. For a diatomic molecule with a harmonic binding potential, the kinetic energy contained in the wave function is half the vibrational energy: $E_{kin} = 1/2\hbar\omega(n + 1/2)$ where $\omega$ is the vibrational frequency of the molecule. The energy released in the Coulomb explosion is $E_{rel} = Q_1 Q_2/r_0$, $r_0$ being the instantaneous bond length of the molecule when it hits the target. The ratio of initial kinetic energy contained in the wave function compared to the kinetic energy picked up in the explosion is then:

$$\frac{E_{kin}}{E_{rel}} = \frac{r_0\hbar\omega}{2Q_1Q_2}(n + 1/2) \tag{2.12}$$

As one can see the effect gets smaller with higher $Z$ atoms (as they usually carry higher charges after the passage through the foil) so the strongest effects can be expected for light molecules. The order of magnitude of this effect are given in table 2.2. One can see that the effect is negligible for most cases. One notable exception is the case of vibrationally excited $HD^+$ which was measured at the TSR and where the quantum mechanical nature of the Coulomb explosion process had to be taken into account [12, 19]. The explosion process without target effects can be calculated quantum mechanically, by projecting the initial wave function onto Coulomb wave functions (which are the continuum solutions of the Coulomb problem). Multiple scattering can be included by reversing equation 2.8, to transform the obtained quantum mechanical $V$-space distribution back to $R$-space and then using the classical simulation on the obtained $R$-space distribution to include multiple scattering.

For polyatomic molecules no easy way to include quantum mechanical effects of the explosion exists. One possible way to include the initial momentum contained in the wave function is by calculating the Wigner distribution (see e.g. [34]) of the wave function and sampling initial

| Molecule | $HD^+$ ($\nu = 1$) | $HD^+$ ($\nu = 6$) | $CH^+$ ($\nu = 1$) | $CH^+$ ($\nu = 6$) |
|---|---|---|---|---|
| $E_{kin}$ | 0.12 | 0.62 | 0.09 | 0.98 |
| $E_{rel}$ | 13.5 | 13.5 | 50.2 | 50.2 |
| $E_{kin}/E_{rel}$ | 0.009 | 0.045 | 0.002 | 0.020 |

**Tab. 2.2:** *Kinetic energy release ($E_{rel}$) and initial kinetic ($E_{kin}$) for some molecules in selected vibrational states $\nu$. For the $CH^+$ ion, the explosion into $C^{4+}$ and $H^+$ was chosen as this is the typical charge state used when measuring this molecule. All energies are in eV, Data taken from [1, 33]*

positions and momenta of the ions in the molecule from this distribution. This approach has some technical difficulties, however, as the Wigner function is not necessarily positive everywhere.

The other quantum mechanical effect which can affect the explosion is interference. Supposing one has a molecule with identical nuclei in it. It is then in principle impossible to tell which of the initial ions hit which spot on the detector. Fortunately, for most molecular ions the ions are well separated in phase space and interference terms are negligible.

## 2.5 Successes

A number of successful and interesting experiments have been performed with the CEI setup in Heidelberg in the last years. The advantage of the setup in Heidelberg is the combination of the Coulomb explosion experiment with the storage ring TSR. The ring allows the storage of molecular ions produced in the ion source for a few seconds before guiding them to the experiment.

Molecular ions are usually produced with a lot of internal excitations in an ion source. A lot of methods have been developed to reduce this excitation, the most successful one being supersonic expansion [35]. But these methods of producing cold ions in the source still have the disadvantage that it is very hard to control the exact experimental conditions. An alternative way to obtain vibrationally cold molecules is to store them somewhere for a longer time than the lifetime of the excited rovibrational states before starting to measure. The molecules will then cool down to a rovibrational distribution in thermal equilibrium with their surroundings at 300 K. This is exactly what can be done with the storage ring. Moreover it allows to study the molecules while they are cooling.

This fact has been used in the measurement of the $HD^+$ molecule. The energy of the $HD^+$ beam in this measurement was 2 MeV. Figure 2.4 shows the width $\Delta V$ of the measured distribution $P(V)$ for $HD^+$ as a function of storage time in the TSR. The decrease of the width is a direct

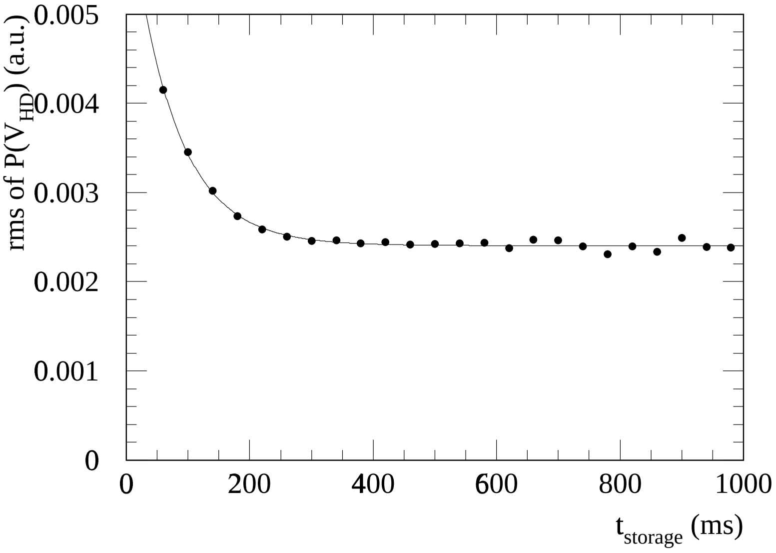

**Fig. 2.4:** *The width of the measured $V$-space distribution $P(V)$ of $HD^+$ as a function of storage time. Picture taken from [14].*

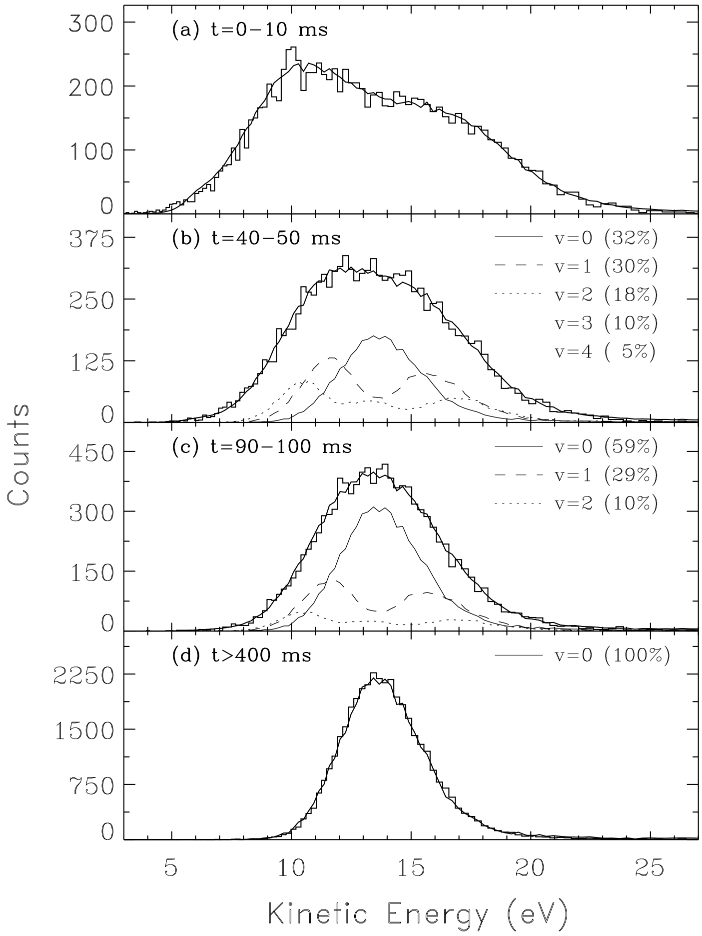

**Fig. 2.5:** *The distribution of kinetic energy $E_{kin}$ between the two fragments of $HD^+$ at different storage times, and the population of the vibrational states fitted to them. Picture taken from [19].*

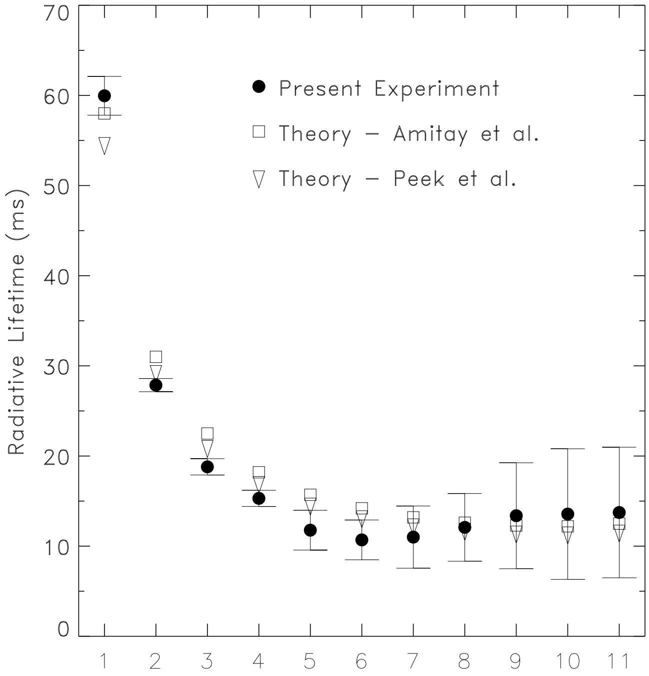

**Fig. 2.6:** *The lifetimes of the different vibrational states of HD$^+$. Round dots are the CEI experiment, open squares and triangles two different theories [36]. Picture taken from [19].*

sign of the cooling of the molecule. After about 300 ms the width does not change anymore, a sign that the molecule has reached thermal equilibrium with its surrounding. Because of the energy difference of about 240 meV [1] between the $\nu = 1$ and $\nu = 0$ states of HD$^+$ which is by far larger than the thermal energy of about 25 meV at room temperature the molecule can be expected to be in its vibrational ground state.

Measuring the $V$-space distribution P(V) as a function of storage time in the TSR allowed to extract not only the structure of the ground state but also the vibrational lifetimes of the excited states of HD$^+$ [12, 19]. This can be done, by taking a series of $V$-space distributions for different storage times and fitting to them a sum of theoretical distributions for each vibrational state of the molecule. In figure 2.5 the measured distribution P(E) for some selected storage times can be seen together with the fit of the theoretical curves. $E$ is the kinetic energy between the two fragments and related to the relative velocity $V$ between the two fragments by $E_{kin} = \mu/2 \cdot V^2$ where $\mu$ is the reduced mass of the system. The distribution for storage times larger than 400 ms agrees perfectly with the vibrational ground state of HD$^+$. To obtain such good agreement a quantum mechanical simulation of the Coulomb Explosion process, as described in the previous section had to be applied to the theoretical wave functions The population of different rotational states in each vibrational state does not change the $R$-space distribution noticeably and can thus not be measured.

Fitting the vibrational population to the distributions measured at different storage times and fitting the obtained vibrational populations to a model using the lifetimes of the different vibrational states as fit parameters, resulted in figure 2.6. As the distribution of rotational states can not be measured, these lifetimes are averages over this distribution. The theoretically computed lifetimes shown in the same figure assume two different populations for the rotational states. As the measured lifetimes agree well to both theoretical calculations the influence of rotational excitations seems to be rather weak.

Another point where is is possible to use the simple Coulomb model is the measurement of bond angles for quasi-linear molecules. For this case it has been shown that the measured bond angle distribution is mostly independent of the exact form of the potential driving the explosion[3, 14]. The difficulties related to measuring the length of a certain molecular bond will be discussed in the next section.

## 2.6 Difficulties

The method does not always work as good as in the examples above. Figure 2.7 shows a measurement of the $DCO^+$ molecule at 3.2 MeV (data taken from [14]). The plots shows the distribution of relative velocities between the carbon and the oxygen ion. The measured charge states had to be restricted to $C^{2+}$, $O^{2+}$ and $D^+$ for technical reasons (higher charge states of Carbon and Oxygen were not clearly separable on the detector). The lines show the result from a simulation carried out with fixed bond lengths. Due to the rigid structure of the CO

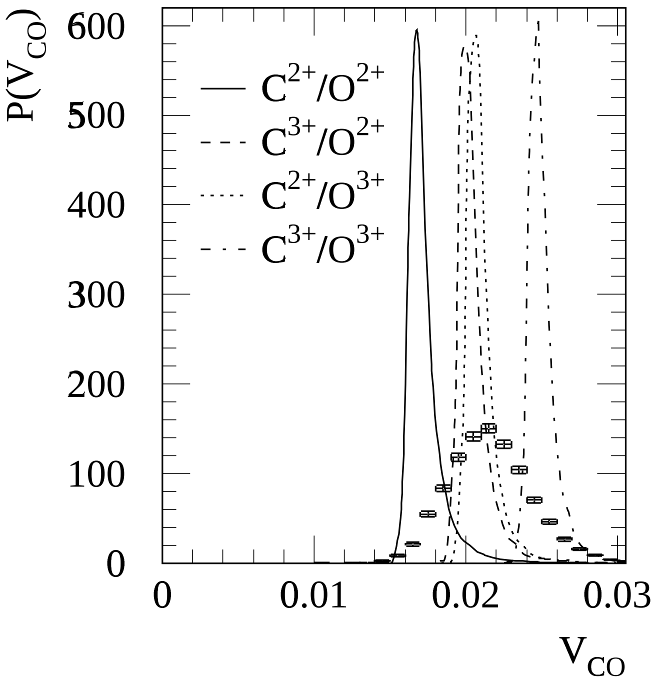

**Fig. 2.7:** *The measured bond length distribution of the $DCO^+$ molecule compared to the expected distribution for a molecule with a bond length fixed to the equilibrium distance. The charge states of the exploding molecule are 2+ for both the carbon and the oxygen fragment. The simulation was carried out for a set of different charge states between 2+ and 3+. Picture taken from [14].*

bond this is a good approximation and the simulation is expected to not look very different if a distribution of bond lengths according to the actual wave function of the molecule would have been assumed. The solid line shows the result for an explosion according to the measured charge states. The dashed, dotted and dash-dotted lines assume higher charge states for the explosion than the ones measured on the detector. It can be easily seen that the measured distribution is by far wider than the one obtained from the simulation. The difference can not be explained by the fact that a fixed bond length had been assumed in the simulation. The second problem is the fact that the simulation of the explosion for the charge states $C^{2+}$, $O^{2+}$ and $D^+$ gives a completely different mean value for the relative velocities than the experiment. The experimental distribution looks more like the explosion happened with a charge state of $C^{3+}/O^{2+}$ or $C^{2+}/O^{3+}$. So the measured charge state seems to be lower than the one according to which the explosion happened. Similar effects could also be seen in measurements of $NH_2^+$ and $CH_2^+$ [37] and were one of the motivations for this work.

For almost linear molecules however the measured angular distribution in velocity space is in first order independent from the exact form of the potential which drives the explosion [14]. It has to be noted that also in the case of $DCO^+$ the measured distribution of the bending angle of the molecule is in agreement with theory [14, 38].

# 3. Experimental approach

The last chapter discussed the general method of Coulomb explosion imaging, some of its successes and some difficulties related to measuring the spatial structure of molecules, especially bond lengths for heavier, not completely stripped molecular ions. This chapter is meant to give an idea how to reach a better understanding of these aspects of Coulomb explosion by systematic measurements. A short description of the molecules used for this purpose will be given.

## 3.1 General idea

As has been shown in section 2.6 the explosion process happening in the foil induced dissociation cannot always be described by a model using pure Coulomb potentials. While the model of a Coulomb explosion works very well when looking at completely stripped molecular ions, it does not work when trying to measure bond lengths of molecules where several electrons remain in the system after the target foil. There are several effects which could cause a change in the measured $V$-space distribution of the molecule (see section 2.4). As was shown there most effects happening inside the foil are described quite well by the current simulation. These effects should not depend on whether one measures naked ions or not completely stripped ions on the detector, since they are happening inside the foil, and the final charge state of the molecular fragments is still not fixed during their passage through the foil.

The two known effects remaining are quantum mechanical effects during the Coulomb explosion and the assumption that the ions are point-like and the explosion follows Coulomb trajectories. As was already discussed in section 2.4 the quantum mechanical nature of the explosion process should not play a significant role for the explosion of heavier molecules as long as no interference comes into play. This leaves, as the only remaining difficulty of the CEI technique, the assumption of point-like ions and the explosion happening on Coulomb trajectories. It has been shown in the previous section that this assumption would hold quite well for most molecules if all the electrons remaining were in the deepest possible bound state of the dissociating ion. If the remaining electrons are however bound in higher excited states the whole picture of point-like ions carrying the final charge state measured on the detector during all of the explosion breaks down.

This breakdown of the approximation of point-like ions has already been seen in quite a few experiments (see section 2.6). Understanding the limits of the current simulation of the CEI process is needed for the further progress of this method of investigating molecular structure. A possible way to achieve a better understanding is to reverse the current approach. If we have a molecule with a known structure the measurement of its Coulomb explosion and the measured deviations from the simulation using Coulomb potentials for the explosion might give some hints about the effects happening and possible ways of dealing with them. Some sort of systematics will be needed, to understand the dependence of the deviations on the measured charge state. It is expected that the Coulomb model will fit for naked ions while strong deviations are expected for low charge states. It will be interesting to see the behavior of intermediate charge states and how far they will fit the Coulomb model.

For this purpose molecules with a well known structure have been selected for these measurements. The simplest molecular ions that can be used are the series of $XH^+$ molecules where X is an arbitrary element. Precise structural data for this molecule should be available from theory or other measurements and the element should not be too heavy to be able to measure the explosion to fully stripped ions. Measuring the fully stripped ion helps verifying that the structure used as an input to the simulation does really correspond to the structure of the measured molecule.

Besides the lightest system, $HD^+$, which has already been presented in [14] and in the last chapter, this work will focus on three of the lightest molecular ions: $HeH^+$, $LiH^+$ and $CH^+$. For both $HeH^+$ and $LiH^+$ it is still possible to measure the explosion into naked ions while this is not possible for $CH^+$, due to technical limitations which do not allow to raise the kinetic energy to a value high enough for this purpose at the TSR. Although all of these ions are composed of a hydrogen atom paired with a heavier atom, their properties differ quite significantly. The next sections will present a short summary of the known properties of each of these molecular ions as far as they are relevant for this work.

Rotational excitations are not discussed in these sections as they do usually not change the measured $V$-space distribution noticeably. As long as the excitation is not too high the shape of the wave function does not change significantly but gets shifted a bit towards larger relative distances between the ions. On the other hand the energy of the rotational excitations is stored in kinetic energy of the two molecules moving around each other. This energy contributes to the kinetic energy released in the dissociation and tends to compensate the shift of the center of the wave function.

## 3.2 HeH$^+$

The HeH$^+$ molecule is one of the simplest molecular ions and thus has been investigated extensively as well theoretically as by experiment [39, 40, 41]. Since the molecule is made up from the two lightest and most abundant elements in interstellar space, the molecular ion should exist in certain astrophysical environments like nebulae [42]. This seems to be in contradiction with the difficulty to observe HeH$^+$ in astrophysical plasmas [43]. This has in the last years triggered a lot of research about the formation and destruction processes of HeH$^+$, especially about the dissociative recombination of this ion (see for example [11] and references therein).

The HeH$^+$ ion is isoelectronic to the $H_2$ molecule and thus quite well known from theory. The bond length at the minimum of the electronic ground state ($X^1\Sigma^+$) is 1.46 a.u. and the binding energy of the ground state is 1.98 eV [44, 45]. The vibrational spacing between the ground state and the first excited state in the $X^1\Sigma^+$ curve is 0.26 eV [39].

Almost all states have lifetimes in the order of 1–5 ms [41]. This is fast enough so that one can assume that all molecules extracted from the storage ring after more than about 100 ms are in thermal equilibrium with the surrounding environment. Since the vibrational spacing is large compared to the thermal energy at 300 K, the thermalized HeH$^+$ molecule should be completely in its vibrational ground state.

## 3.3 LiH$^+$

Little is known experimentally about the LiH$^+$ molecular ion. To the best of our knowledge the measurement to be shown in this work represents the first time that this molecule has been produced and investigated experimentally. There does however exist some theoretical work on this ion which is summarized in the following.

LiH$^+$ is a quite unusual molecule because of its large bond length of 4.25 a.u. and its very small binding energy of only about 0.115 eV. The shallow potential only supports a total of 6 bound vibrational states [46]. A sketch of the ground potential curve and the bound vibrational states inside is found in fig. 3.1. The potential surface was calculated in [46] and the vibrational levels are calculated using the Level program [47]. The low vibrational spacing implies that even in thermal equilibrium at room temperature the molecule is not purely in the vibrational ground state. About 20% of the molecules occupy the first vibrational state and about 2% are even found in $\nu = 2$.

The lifetimes of the different vibrational states have been estimated to be of the order of seconds [48] and are shown in Table 3.1. The lifetime calculations were done using the transition matrix elements for the vibrational transitions from [49] and the Level spacing given by the

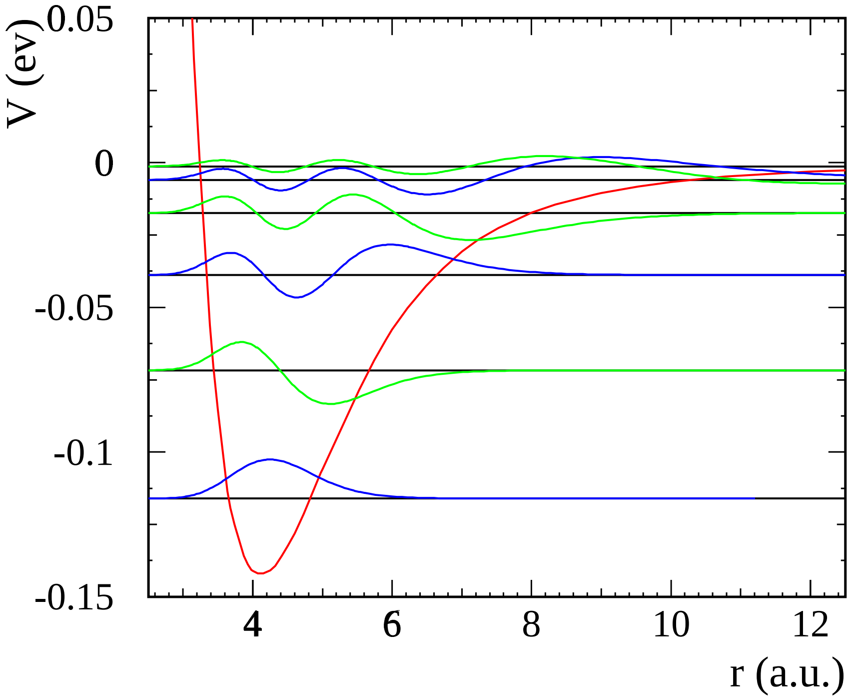

**Fig. 3.1:** *The potential curve of the LiH$^+$ molecule, and the bound vibrational states inside this molecule.*

Level program [47]. The long lifetimes imply that it will not be possible to measure the molecular ions relaxed to thermal equilibrium. The LiH$^+$ molecular ion has a couple of other weakly bound electronic state but all of them have a average bond length of about 8 to 20 a.u. [46], and have not been seen in our measurement.

## 3.4 CH$^+$

The CH$^+$ ion has raised a lot of interest in the last years, mainly because the ion plays a key role in the chemistry of cold interstellar and planetary clouds [50]. The measured abundancies of CH$^+$ in these clouds do not agree with theoretical models of the processes happening in these clouds.

| Vibrational state $\nu$ | 1 | 2 | 3 | 4 | 5 |
|---|---|---|---|---|---|
| Lifetime [s] | 2.5 | 2.4 | 4.8 | 20.8 | 333.0 |

**Tab. 3.1:** *Estimated lifetimes of the $\nu \to \nu - 1$ transitions in LiH$^+$ (data from [48]).*

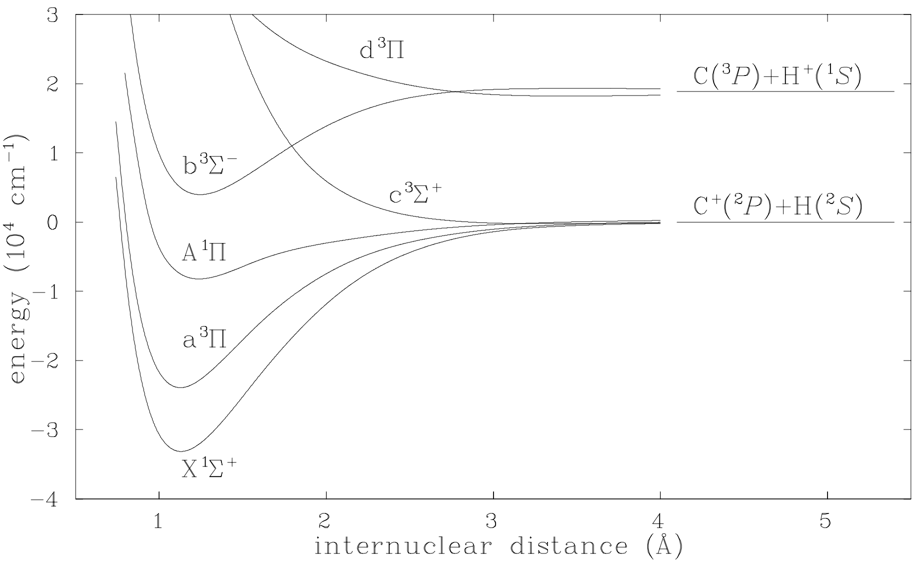

**Fig. 3.2:** *The potential curves of the CH$^+$ molecule. The* a$^3\Pi$ *state is metastable with a lifetime of about 7 seconds.*

Several bound electronic states of the molecule exist and are shown in figure 3.2. The ground state of CH$^+$ (X$^1\Sigma^+$) is very well known and has been extensively studied [51, 52]. The equilibrium bond length is $R_e = 1.127$ Å and the dissociation energy is 4.08 eV [53]. The vibrational constant amounts to 0.344 eV. Theoretical calculations for the lifetime of excited rovibrational levels of the X$^1\Sigma^+$ state [54] have predicted a lifetime of 710 ms for the slowest vibrational transition (from $\nu = 1$ to 0) in CH$^+$. Thus one can expect full vibrational relaxation of the ion to occur in the first few seconds of storage in the ring.

There is however a meta-stable electronic state (the a$^3\Pi$ state), with a lifetime of around 7 seconds and an initial population of about 60–70% [10]. The structural properties of this state are, with an equilibrium bond length of $R_e = 1.130$ and a vibrational constant of 0.313 eV almost identical to the electronic ground state. The vibrational relaxation time inside the a$^3\Pi$ state has been measured to be of the same order of magnitude as for the ground state, and shorter than the lifetime of the a$^3\Pi$ state [10]. Since this state has almost the same structural properties as the ground state it is not possible to distinguish between these two states in CEI measurements. The lifetimes of the other electronic states of the molecule are quite short and are thus unimportant in the CEI measurement of this molecule.

# 4. Experimental setup

This chapter will focus on the experimental setup used at the Coulomb explosion imaging experiment in Heidelberg. The setup has already been described in a recent publication [13], and the description here will only summarize the most important points. The following sections will focus on the different parts used in the experiment. The accelerator and the ion source which produce the ion beam, the storage ring TSR where the ions are stored for several seconds, the extraction beam line which transfers the ions to the CEI experiment and finally the experimental setup itself.

## 4.1 Production, acceleration and storage of molecular ions

At the accelerator facility of the Max-Planck-Institute für Kernphysik in Heidelberg three different accelerators exist that can be used to produce fast molecular ion beams. Two of the accelerators are purely electrostatical, a single ended van-de-Graaff and a Tandem accelerator. The third accelerator, referred to as the high current injector (HCI), consists of two radio frequency quadrupole (RFQ) structures followed by two seven-gap resonators. Due to the different ways the accelerators are build up and the different sources attached to them, each of them has certain advantages and disadvantages for producing molecular ions.

The terminal of the van-de-Graaff is equipped with a penning source and can produce positively charged ions. The accelerator can reach a maximal terminal voltage of about 2.5 MeV. In the last years a number of different molecules have been produced in this accelerator, see [14]. One can usually get molecular ion beams with currents of about $1\,\mu$A from this source. The disadvantage of this accelerator is the limitation to 2.5 MeV which is often too low for Coulomb explosion imaging experiments one wants to perform. It could however be used for the measurement of $HD^+$ presented in section 2.5.

The second accelerator is a 12 MV Tandem. Molecular ions are produced by first producing negative ions on a platform. These are then accelerated to the terminal of the tandem where the desired positive molecular ion is produced in a gas target. This can be done either by the stripping of two electrons or by breakup of the negative ion. The breakup procedure can be

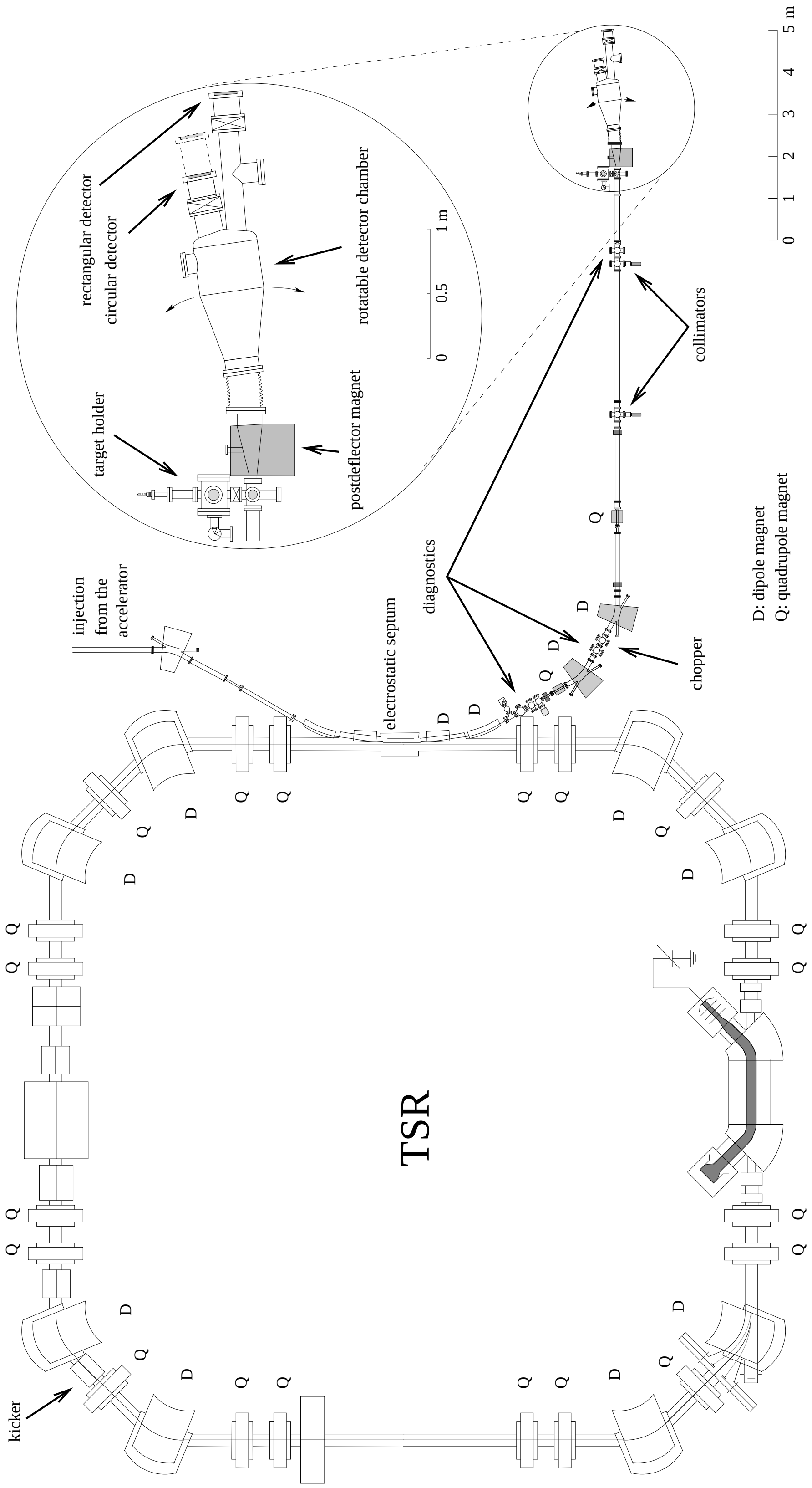

**Fig. 4.1:** *The heavy ion storage ring TSR together with the injection beam line and the Coulomb explosion imaging experiment. Enlarged is shown the location of the CEI target, the post deflector and the imaging detectors.*

| Accelerator type | Molecular ion beam | Total energy | Beam intensity | Precursors |
|---|---|---|---|---|
| van-de-Graaff | $HD^+$ | 2.0 MeV | 1 $\mu$A | HD |
| Tandem | $CH^+$<br>$LiH^+$ | 6.5 & 4.0 MeV<br>6.5 MeV | 25 nA<br>150 pA | $CH^-$<br>$LiH_2^-$ |
| RFQ | $^4HeH^+$ | 2.4 MeV | 100 nA | $^4He + H_2$ |

**Tab. 4.1:** *Summary of the molecular ion beams presented in this work.*

used to produce positive ions which do not have a stable negatively charged counterpart. The then positively charged ions get accelerated once again from the terminal to the exit of the tandem. There are two different sources for producing negative ions: a Cesium sputter source and a duoplasmatron source. In the experiments presented in this work $CH^-$ was produced in the sputter source and stripped to $CH^+$ on the terminal of the Tandem. $LiH^+$ on the other hand was produced with the help of a $LiH_2^-$ beam which was broken up into $LiH^+$ and a Hydrogen. The disadvantage of this way of producing molecular ions are the low currents obtained. Typical currents are usually in the order of nano- to picoamperes due to the small cross sections for ionisation in the gas target. Working with such low current beams in the storage ring usually requires an atomic pilot beam with the same charge to mass ratio to be able to setup the ring and the extraction.

The third accelerator, the high current injector (HCI), uses two RFQ structures for accelerating the ions. Like in the van-de-Graaff one can directly use positive ions and thus achieve higher currents. Because the accelerator is build out of a cavity and uses a fixed frequency radio frequency field, it always produces ion beams of fixed velocity, in this case with 3.3% of the speed of light (500 keV/a.m.u.). By turning off one of the two cavities, one can also reach half the energy, corresponding to 2.3% c. Using the seven gap resonators positioned after the two RFQ structures or the post accelerator one can further increase the velocity. The main limitation of the HCI is the fact that the maximal mass to charge ratio is limited to 9 which for singly charged molecular ions limits the total mass to 9 a.m.u. Thus the accelerator can only be used for the lightest molecular ions.

From the accelerators the molecular ion beam can be transfered to the storage Ring TSR. The heavy ion storage ring TSR is used for molecular physics experiments because of its capability to produce internally cold molecular ions. Apart from Coulomb explosion experiments concerning dissociative recombination and photo dissociation were performed (see e.g. [10, 12, 55]). The basic magnetic structure of the TSR consists of eight dipole, twenty quadrupole and twelve sextupole magnets that form a ring with a circumference of 55.4 m. An electron cooler in one section can be used to cool the ion beam translationally and to perform recombination

experiments.
The ion beam is injected into the ring at the electrostatic septum, using a multi turn injection which increases the current stored in the ring by up to a factor of 40 compared to the current of the injected ion beam. The typical vacuum in the ring is at about $3 \cdot 10^{-11}$ mbar and gives beam lifetimes for molecular ions of about 10–30 seconds. Molecules with masses from 2 to 44 have already been stored in the ring with beam currents between 40 $\mu$A for $HD^+$ and about 1nA for $D_2CO^+$. Below 1 $\mu$A measurements of the absolute current are not possible, and below 10 nA the beam current is not measurable anymore, so that the $D_2CO^+$ ions could not be detected inside the ring. With the help of the relation

$$I_{\mathrm{TSR}} = N_{\mathrm{TSR}} q_{ion} v_{ion} / L \tag{4.1}$$

one can calculate the number of ions $N_{\mathrm{TSR}}$ stored in the TSR, for a typical current of molecular ions $I_{\mathrm{TSR}} = 100\,\mathrm{nA}$, a velocity $v_{ion}$ of about 2% of the speed of light and the circumference $L$ of the TSR to about $5 \cdot 10^6$ stored particles.
The maximum momentum of ions which can be stored is limited by the maximum magnetic field of the dipole magnets in the TSR. Setting the Lorentz force acting on the ions equal to the centrifugal force acting on them on a circular path with radius $\rho$ gives:

$$\frac{m_{ion} v_{ion}^2}{\rho} = q_{ion} v_{ion} B \quad . \tag{4.2}$$

Solving for $v_{ion}$ of singly charged ions one does get the following expression for the maximum ion velocity as as function of rigidity ($B\rho$) and the ion mass:

$$v_{ion} = \frac{B\rho}{m_{ion}} = 0.322c \times \frac{B\rho[\mathrm{Tm}]}{m_{ion}[\mathrm{a.m.u.}]} = 44.2\mathrm{a.u.} \times \frac{B\rho[\mathrm{Tm}]}{m_{ion}[\mathrm{a.m.u.}]} \tag{4.3}$$

Since the maximum rigidity of the TSR is 1.5 Tm, and one needs ion velocities of more than 1 a.u. to get reasonable stripping in the target, CEI experiments at the storage ring TSR are limited to single charged ions with a mass of less than 40 a.m.u.
To be able to measure the molecules with Coulomb explosion imaging one has to extract them again from the storage ring and direct them onto the experiment. To achieve this a part of the stored ion beam is continuously extracted from the TSR using a slow extraction technique [56, 57]. In this slow extraction technique the working point of the TSR is set close to a 3rd order resonance which means that the ratio of the horizontal betatron frequency to the revolution frequency is close to an integer divided by three. This is done by using the sextupole magnets in the storage ring and leads to a significantly reduced region in horizontal phase space where the beam is stored. Injected ions are still stored in the stable region of the phase space but by applying an external transverse RF field to the beam one can increase the amplitude of the

betatron oscillations and push the ions out of the stable phase space region. After this point the ions get driven away from the stable phase space region with increasing velocity and after a few revolutions their distance to the stable orbit is large enough to be able to separate them from the main beam. This is done with the same electrostatic septum that is already used for injecting the beam into the ring. If the ions get inside the septum, they are deflected away from the beam with a transverse electrostatic field of about 20kV/cm. They are then guided and deflected away from the TSR by two additional dipole magnets, the magnetic septa.

By changing the amplitude of the RF field applied to the ions in the ring one can control the rate of extracted ions from the ring. Since the CEI experiment can only handle a rate of 25 events per second one can increase the lifetime of the ions in the ring and the period over which particles are extracted by switching the RF field off, once a molecule has hit the detector, and turning it back on as soon as the detector is ready again to measure the next event. The efficiency of extraction, defined as the amount of particles successfully extracted divided by the number of particles stored, is about 25% [58]. This is mainly due to the ion beams high vertical temperature which results in most of the extracted ions getting lost in the small aperture of the extraction channel. When using the electron cooler to first cool the ion beams down to a low temperature and then extracting them an efficiency of about 80% could be reached [58].

## 4.2 Coulomb explosion imaging setup

After extracting the beam from the TSR it is guided through the extraction beam line onto the experiment. The experiment allows to measure the final velocities of all fragments emerging from the Coulomb explosion target, one molecule at a time. To get single molecules onto the detector a fast electrostatic chopper is used, built up as a parallel plate capacitor with 5 kV maximum voltage and 500 ns switching time. This deflector is controlled by the data acquisition electronics and will deflect the beam once a particle hits the detector. Because

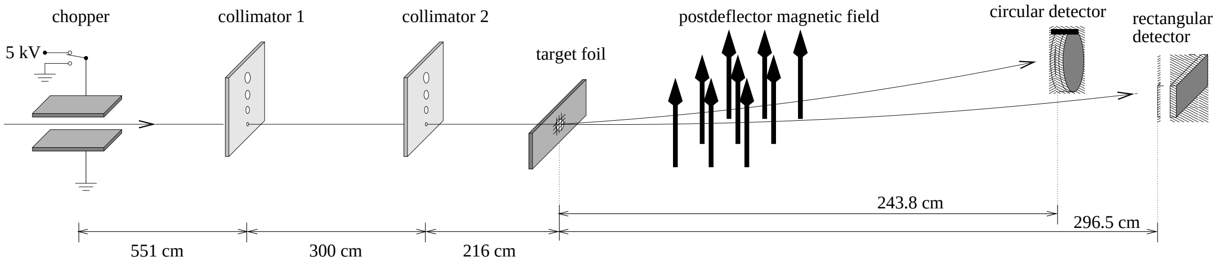

**Fig. 4.2:** *The setup of the Coulomb explosion imaging experiment at the TSR with the CEI target, the electrostatic chopper and the collimators upstream of the target and the post deflector magnetic field and the multi-particle three-dimensional imaging detectors downstream of the target.*

of its fast switching time and the low rate of extracted ions the detector will only see single molecule events.

After the chopper, the ion beam is passed through two collimators (0.5 to 5 mm diameter; 3 m apart) which allow to reduce beam divergence down to ±0.17 mrad. Two meters behind the second collimator the beam enters the vacuum chamber that contains the Coulomb explosion target. With the help of a linear motion feed through, eight different targets can be inserted into the beam. Two different types of target foils are used in the experiment, both with thicknesses below $1\,\mu g/cm^2$. The first type of target is made out of Formvar resin which has been used for many years to produce chemically stable targets [59]. With a density of about $1.2\,g/cm^3$, a target of $1\,\mu g/cm^2$ amounts to a thickness of about 80 Å. With Formvar it is very hard to produce targets thinner than about $1\,\mu g/cm^2$. A recently introduced alternative are diamond-like carbon (DLC) foils which are made available by V. Liechtenstein (RRC Kurchatov Institute, Moscow) [60]. These foils have a density of about $2\,g/cm^3$ and can be produced with less surface density. The thinnest target foils produced have a surface density of about $0.5\,\mu g/cm^2$, resulting in a thickness of only 25 Å [61]. There are two advantages of using these foils compared to the Formvar ones. The smaller surface density reduces multiple scattering and the even more reduced geometrical thickness has the effect that a smaller fraction of the explosion takes place inside the foil. The second advantage is that the amount of pinholes in the target is much smaller for DLC targets than for Formvar, resulting in an improved efficiency of the experiment. Because of these reasons DLC targets have almost completely replaced the old Formvar targets in recent experiments. For the measurement of $HeH^+$ as well as $LiH^+$ a Formvar target with a thickness of 0.7 $\mu g/cm^2$ was used while the $CH^+$ experiment was performed with a DLC target of about 0.5 $\mu g/cm^2$.

After the target the resulting fragment ions are deflected according to their charge to mass ratio inside a dipole magnet, the post deflector which is located behind the target. After drifting another 2–2.5 m each fragment hits one of the two detectors. These detectors are capable of detecting multiple particles at the same time, and are used to measure the final velocities of all fragments. The detectors are positioned on an arc around the center of the post deflector, and have a fixed angle of 120 mrad between them. The support holding the two detectors can be turned by up to 300 mrad around the post deflectors center. The variable position of the detector system together with the adjustable magnetic field allows to measure many different molecular systems at different beam energies. The light fragments (protons or deuterons) are usually deflected onto the detector further away from the beam axis, the heavy particles (Nitrogen, Carbon, Oxygen in different charge states) are measured on the detector closer to the beam axis.

The velocities of the fragments to be measured on the CEI detectors are of the order of 0.01

to 0.05 a.u. in the center of mass frame of the dissociating molecule which is small compared to their velocity in the laboratory frame, typically between 2 and 5 a.u.. Typical transverse distances on the detector are therefore a few centimeters while time differences are of the order of a few nanoseconds. These values show that a detector used for CEI experiments has to be able to measure the impact of multiple particles with a spatial resolution of less than a millimeter and a time resolution in the sub nanosecond regime.

## 4.3 Data acquisition

The two detectors used in the setup are build up in a very similar way with the main difference being their different size and geometry. A schematic view of the round detector and its readout electronics can be found in figure 4.3. The rectangular detector for heavy particles is operated in a similar way. The detector system used at the CEI setup has been developed at the Weiz-

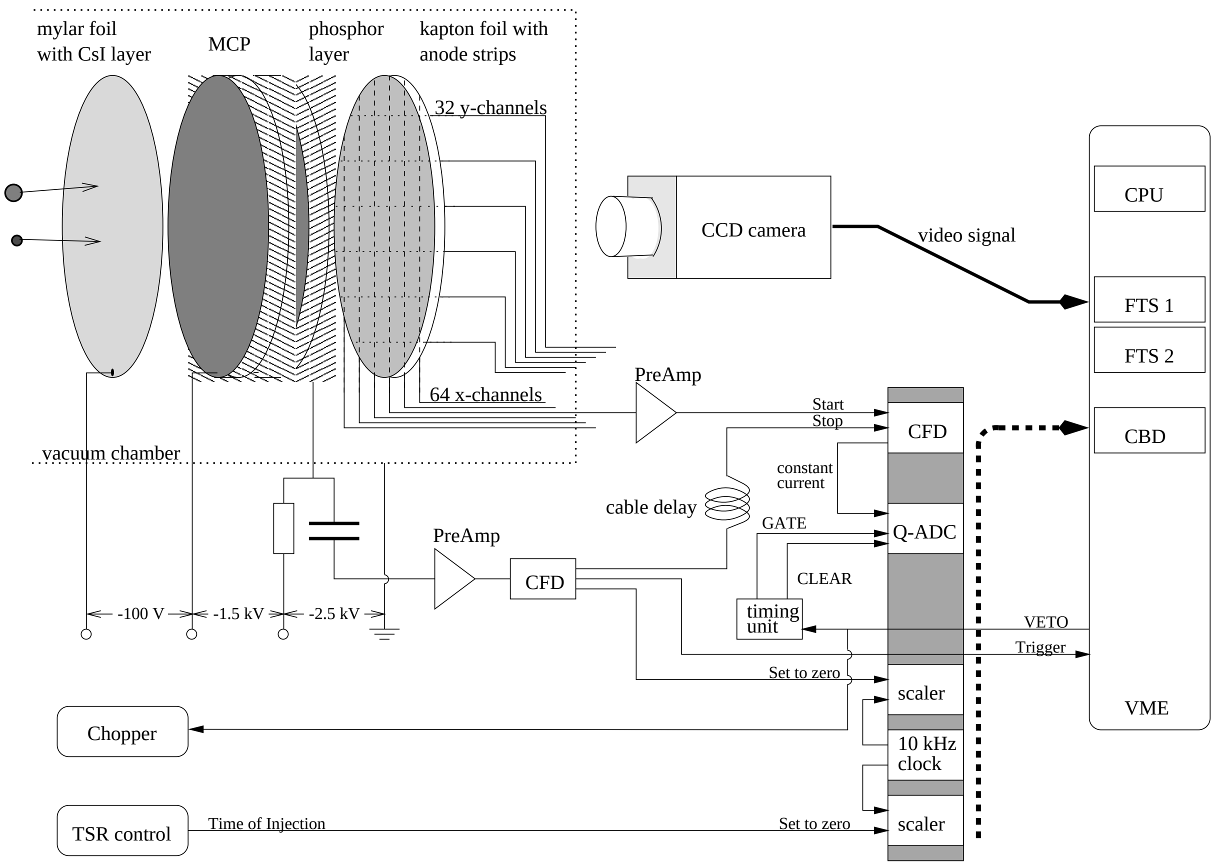

**Fig. 4.3:** *Schematic view of one of the 2 detectors of the Coulomb explosion imaging experiment including the electron-ion conversion foil, the MCP and the phosphor layer with anode strips below. A CCD camera does the readout of the transverse positions while the signals from the anode strips is fed into the CFD/Q-ADC combination to measure time differences of the different fragments.*

mann Institute of Science and is an improved version of the setup used at the CEI experiment there [62]. Both detectors consist of an ion-electron conversion foil, a two stage micro channel plate (MCP) in chevron layout, a phosphor screen and a set of anode strips. The active area of the detector is given by the size of the micro channel plates and is 118 mm in diameter for the round detector and $76 \times 93\,\mathrm{mm}^2$ for the heavy particle detector. The conversion foil is build up from a $1.5\,\mu$m Mylar foil coated with a 3000 Å layer of CsI. Ions hitting the detector release a number of electrons when they traverse the CsI which are then accelerated by a voltage of about 100 V between the foil and the MCP. Due to the conversion foil the efficiency of the MCP which is usually at about 50% could be raised to nearly 100%. In the MCP the initial electron pulse is further amplified and after the channel plate one has a pulse of about $10^7$ to $10^8$ electrons which are now accelerated towards the phosphor screen. On the phosphor screen the electrons create a visible light spot with a size of a few hundred micrometers. The light spots are recorded with a CCD camera with 25 Hz frame rate. From the frame picture the transverse impact positions of the particles can be determined. The video signal from the cameras watching the two detectors is digitized by two Frame Threshold suppressors (FTS) developed at the Weizmann Institute of Science [62]. For each video frame the FTS computes a list of pixels that have passed an adjustable intensity threshold. This pixel information is then used to compute the centers of the light spots seen on the detector. The accuracy of the position measurement has been estimated by the intensity profile measured with the CCD to be about 100 $\mu$m which has recently been confirmed by a study of the CEI detectors using laser pulses instead of ions [63].

The impact times of the fragments on the detector are measured using sets of anode strips below the phosphor layer. The anode strips have been etched from a copper layer on a thin optically transparent capton foil. A pulse of electrons hitting the phosphor screen induces a fast signal on the adjacent anode strips. By measuring the time difference between the signals on the anode strips and a common reference signal, the relative impact times of all fragments can be determined. The first particle hitting the MCP will induce a signal on the backplane of the MCP which is then delayed and taken as the common reference signal. The rectangular detector is equipped with 186 parallel, equally spaced anode strips which are oriented perpendicular to the deflection direction of the magnetic field. Each strip is $100\,\mu$m wide and the centers of the strips are 0.5 mm apart. Outside the active detection area, these strips are combined to 93 channels. For the circular detector 128 equally spaced anode strips ($100\,\mu$m wide, 0.925 mm distance between the centers) are located behind the phosphor layer and also oriented perpendicular to the magnets deflection direction. On the backside of the capton foil of the circular detector, an additional set of 96 anode strips ($100\,\mu$m wide, 1.25 mm distance between the centers) are mounted perpendicular to the ones on the front side, i. e. parallel to the deflection direction of the magnet. The strips on the circular detector are then combined to form 64 channels from the strips on the front side of the capton foil, and 32 channels from the backside. The anode plane on the backside of the capton foil increases multi particle efficiency, because it allows one to deduce timing information even for events where two particles hit the same anode strip in the first anode plane. To measure the time difference between the anode signals and the common reference all anode channels are preamplified, and then fed into CAMAC constant fraction discriminators (CFD). For a signal above a programmable threshold the CFD starts at the trigger point to charge a CAMAC Q-ADC with a constant current. The reference signal from the backplane of the MCP is amplified and passed to another CFD. The output is delayed by a few nanoseconds and used as a common stop signal to stop the current flow of all CFDs at the same time. The accumulated charge in the ADCs is digitized and is then proportional to the time difference between the corresponding anode signal and the common stop. The common stop signal is also used to trigger the data acquisition system which suppresses further ion impacts by switching the chopper and starts the digitization of the charges in the ADCs. With the CEI detectors at the TSR typical time resolutions of 100–150 ps (FWHM) for the rectangular detector and 180–250 ps (FWHM) for the round detector have been obtained from measuring single particle hits. The detector study with laser pulses did however indicate that the resolutions obtained for two particles hitting the same detector are up to a factor of 1.5 larger [63]. Further analysis showed that this effect could be explained by cross talk of the preamplifiers for the different channels. Newly build up fast preamplifiers seem to avoid these problems and do now give time resolutions of about 60–70 ps (FWHM) for the rectangular detector, even for multi particle hits.

In the analysis the timing information obtained from the different anode strips is correlated to the position information obtained from the CCD camera, so that each fragment can be assigned two transverse impact positions and one relative impact time.

In addition to the impact times and positions of all the fragments for each Coulomb explosion event the time between the injection into the storage ring (which is up to a few microseconds equal to the production time of the ions) and the impact time onto the detector is determined. For this purpose a 10 kHz clock is used to continuously increment two counters on two CAMAC scaler units. One channel is reset to zero upon injection into the storage ring and gives the exact readout time. The other channel is reset at the time the molecule hits the detector and thus gives the time difference between the hit and the readout of the data. Combining both data gives the impact time of the molecule onto the detector with 100 $\mu$s resolution.

The data read out and storage is performed by a VME computer. Read-out is started when the FTS modules have finished the digitalization of the video frame. The VME does then read the pixel list from the FTS modules, the timing information from the Q-ADCs and the scaler values. If an event trigger occurred and the list of pixels is not empty the event is accepted as a raw data event and stored on the VMEs hard disk. After readout the VME reactivates the FTS and Q-ADC and opens the chopper to let the next molecule pass through to the detector. This measurement cycle is independent of the injection cycle of the storage ring, so in the long run the measured events are uniformly distributed over all storage times.

## 4.4 Detection efficiencies

The efficiencies of the detector are not completely homogeneous over the whole area of the MCPs but decreases towards their edges. For a calibration using an $\alpha$-source the impact positions of the particles on the detector are randomly distributed on the detector plane. One can estimate the relative efficiency of the detector as a function of the impact position of the fragment on the MCP by counting the number of detected hits per area on the detector. For the round MCP the detection efficiency is in a good approximation only dependent on the radial distance from its center. Such a measurement gives the result shown in figure 4.4 where the relative detection efficiency of the round detector is shown as a function of distance from its center. The plot is normalized to one for the central region of the detector. It can be seen that the detection efficiency is almost constant for the inner region of the detector but shows a linear decrease

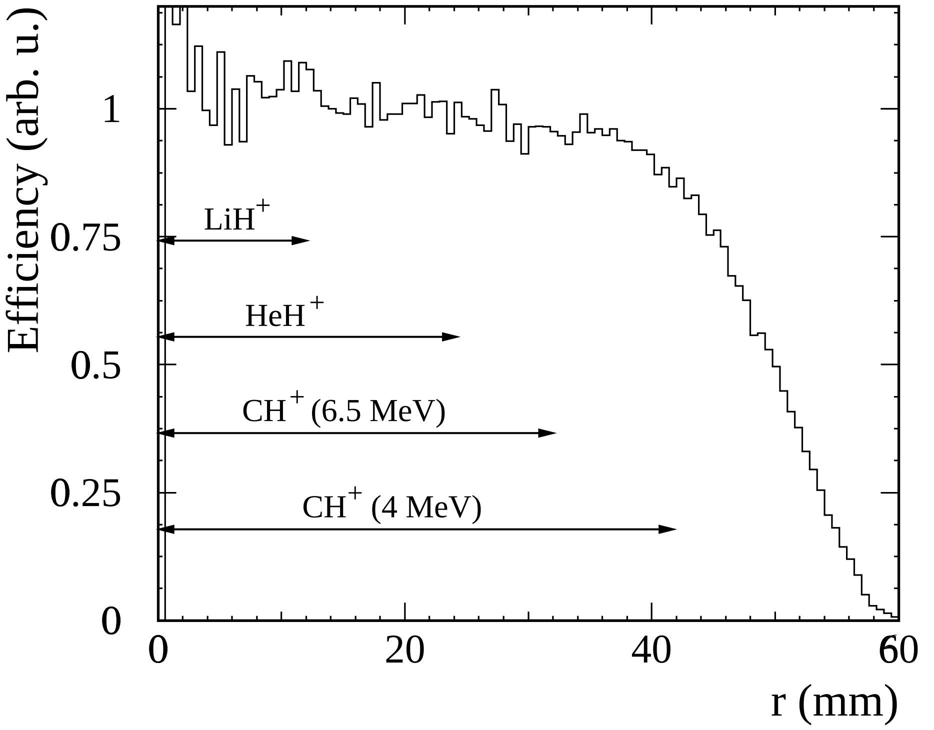

**Fig. 4.4:** *Efficiency of the round detector as function of radial distance r from the center. The central region of the detector is normalized to one. The arrows show the regions used for the different measurements presented in this thesis.*

at distances larger than 40 mm from the center. Most measurements performed in this thesis do only use the inner region of the detector where the detection efficiency is flat. Only in the $CH^+$ data measured at 4 MeV the explosion cone of the Hydrogen fragments was big enough to reach the outer regions of the detector.

A similar picture can be seen towards the edges of the rectangular detector, but all of the data shown in this thesis was measured in the inner region of the detector. To summarize, only in the case of $CH^+$ measured at 4 MeV a correction for detection efficiencies of the MCPs was needed.

## 4.5 Data extraction

A program on the VME computer identifies clusters in the list of non empty camera pixels. A cluster is a number of adjacent non empty pixels with a definable minimum number of pixels and a minimum total intensity. For each cluster the position of its center is determined. This list of centers together with the list of anode strips showing a hit is then passed to a Linux PC for further analysis. The PC uses a calibration done in a separate measurement to transform ADC values of the anode strips to time differences and pixel coordinates on the camera to millimeters.

The calibration is done using single particle hits on the detector. These single particle hits can be obtained in two ways: By using an alpha source or by using a gold foil instead of the regular Coulomb explosion targets. The mean scattering angle in the gold foil is so large that usually only one of the fragments of the molecule hit the detector. By correlating the camera clusters to the hits on the anode strips using the known distance between the strips the conversion factor from pixels on the camera to millimeters on the detector can be obtained. The conversion factor from ADC channels to picoseconds can be obtained by measuring single particle hits with different known time delays for the stop signal.

The coordinate system used in velocity space is defined such that the $z$ axis is parallel to the original beam direction. The $x$ axis is parallel to the deflection direction of the post deflector and the $y$ axis is perpendicular to the deflection direction.

Because of the magnetic field fragments with different charge to mass ratios hit different regions on the detector or different detectors. The deflection of the post deflector is to a good approximation only dependent on the magnetic field and the charge to mass ratio of the fragment. Basically it adds a constant offset in $x$ direction to the explosion cones of each type of fragment. Deviations from this simple model will be discussed below. Since the offsets cannot be deduced with the desired precision from the known values of the magnetic field and the geometry of the detector these offsets are usually derived from the experimental data by calculating the

centers of the explosion cones. This can be done by averaging over all fragments belonging to a certain cone or with the help of a fit function. Usually the latter method is preferred because the detector often has small regions with reduced detection efficiency, so averaging over the fragments could give wrong results.
Another offset must be applied to the timing information because the two detectors are not at exactly the same distance from the target so there is a constant time difference between the impact times of the two fragments on the two detectors. This time has to be determined experimentally because of the different transit times of the signals in the wires by moving the mean time measured for each particle to zero.
After removing these offsets the connection between impact position and impact time of the fragment $i$ on the detector and its velocity in the center of mass frame of the dissociating molecule is given in first order by

$$\begin{pmatrix} V_x^i \\ V_y^i \\ V_z^i \end{pmatrix} = \frac{v_{\text{ion}}}{L} \begin{pmatrix} x^i \\ y^i \\ v_{\text{ion}} t^i \end{pmatrix} \quad . \tag{4.4}$$

L is the distance between target and the detector, where the fragments are measured.
There is a small additional correction that needs to be done for stronger magnetic fields. In the magnetic field a mixing between the $x$ and the $z$ coordinates occurs. This is due to the fact that slower particles are deflected stronger in the field. The effect can be described in terms of a mixing matrix between $x$ and $z$:

$$\begin{pmatrix} V_x^i \\ V_z^i \end{pmatrix} = A \begin{pmatrix} V_x^{i,meas} \\ V_z^{i,meas} \end{pmatrix} \quad , \tag{4.5}$$

where $A$ is a $2 \times 2$ matrix. $A$ can be either fitted directly from the data or to the data obtained from the tracking simulation through the detector. Fitting to the experimental data is done by looking at the experimental distribution in the $V_x$-$V_z$-plane, which should be (except for different resolutions in $x$ and $z$ direction) spherically symmetric. In the simulation one can directly compare the $V$-space distribution before the magnet with the distribution extracted from the simulated impact times and positions on the detector and compare the deviations on a particle by particle basis. Depending on the quality and available statistics of the experimental data either of the methods gets used. In this work the correction had to be applied to the $\mathrm{CH}^+$ measurements and to the part of the $\mathrm{HeH}^+$ data that was measured using two detectors. The $\mathrm{LiH}^+$ molecule was measured on one detector only. Because small deflection angles chosen in this case a correction for the $x$-$z$ mixing was not needed. This does also apply to the $\mathrm{HeH}^+$ data measured with one detector only.

After applying these transformations one arrives at a set of 3N velocities $(V_x^1, V_y^1, V_z^1, V_x^2, ...V_z^N)$ for each event. As in this work diatomic molecules are examined one ends up with 6 coordinates in $V$-space. Three of these coordinates are related to the center of mass motion of the fragments and can be removed by looking at the velocity difference $\mathbf{V} = \{V_x, V_y, V_z\}$ between the two ions.

$$\mathbf{V} = \mathbf{V}^1 - \mathbf{V}^2 \tag{4.6}$$

In this thesis fragment number one is always the heavier fragment.

Measuring many events on the detector will then lead to a probability distribution in velocity space, the $V$-space distribution. For diatomic molecules this distribution will depend on the three components of the relative velocity and is usually written a $P(V_x, V_y, V_z)$. For most of the data analysis a different set of coordinates is more convenient:

$$V = |\mathbf{V}| \tag{4.7}$$

$$\cos\Theta = V_z/V \tag{4.8}$$

$$\Phi = \mathrm{atan}\,(V_y/V_x) \cdot \mathrm{sgn}(V_x) \tag{4.9}$$

If $\mathbf{V}$ is the relative velocity of the fragments then $V$ gives the absolute value of the relative velocity. This is the physically interesting quantity, as its distribution is directly related to the distribution of bond lengths in the molecule before the explosion.

$\Theta$ gives the angle between the vector of relative velocity and the detector plane. If one projects $V$ onto the detector plane then $\Phi$ is the angle of this projected vector to the $x$ axis. These two values give the orientation of the molecule when hitting the target foil, and can be used to investigate detector and target effects.

The $V$-space distribution $P(V_x, V_y, V_z)$ does then transform to a distribution $P(V, \cos\Theta, \Phi)$. In the analysis $P(V)$ will be used as a shortcut for the projection of the distribution onto the relative velocity $V$:

$$P(V) = \int_{-1}^{1} \mathrm{d}\,(\cos\Theta) \int_{0}^{2\pi} \mathrm{d}\Phi \, P(V, \cos\Theta, \Phi) \tag{4.10}$$

Similar projections onto the other coordinates will be used too.

## 4.6 Accuracies

The accuracies with which the relative velocities can be measured are limited by the resolution of the detector and the accuracy of its calibration. Since the detector has different resolutions for the transverse impact positions and the time differences the accuracy of the $V$-space distribution will depend on the orientation of the molecule in $V$-space.

In $x$ and $y$ direction the position of each individual event is obtained by transforming the center of the cluster measured in pixel coordinates on the camera to millimeters using conversion

| | | $HeH^+$ | $LiH^+$ | $CH^+$/6 MeV | $CH^+$/4.5 MeV |
|---|---|---|---|---|---|
| conversion accuracies | $V^I_{x,y}$ | $5.6 \cdot 10^{-3}$ | $5.6 \cdot 10^{-3}$ | $4.4 \cdot 10^{-3}$ | $4.4 \cdot 10^{-3}$ |
| | $V^I_z$ | $1.4 \cdot 10^{-3}$ | $1.4 \cdot 10^{-3}$ | $1.4 \cdot 10^{-3}$ | $1.4 \cdot 10^{-3}$ |
| | $V^{II}_{x,y}$ | $9 \cdot 10^{-3}$ | $9 \cdot 10^{-3}$ | $7.5 \cdot 10^{-3}$ | $7.5 \cdot 10^{-3}$ |
| | $V^{II}_z$ | $1.4 \cdot 10^{-3}$ | $1.4 \cdot 10^{-3}$ | $1.4 \cdot 10^{-3}$ | $1.4 \cdot 10^{-3}$ |
| center of single hit | $V^I_{x,y}$ | $1.8 \cdot 10^{-3}$ | $3.5 \cdot 10^{-3}$ | $3.1 \cdot 10^{-3}$ | $2.5 \cdot 10^{-3}$ |
| | $V^I_z$ | $1.9 \cdot 10^{-2}$ | $2.4 \cdot 10^{-2}$ | $1.0 \cdot 10^{-2}$ | $0.6 \cdot 10^{-2}$ |
| | $V^{II}_{x,y}$ | $2.7 \cdot 10^{-3}$ | $5.3 \cdot 10^{-3}$ | $4.7 \cdot 10^{-3}$ | $3.7 \cdot 10^{-3}$ |
| | $V^{II}_z$ | $< 1.9 \cdot 10^{-2}$ | $< 2.4 \cdot 10^{-2}$ | $< 1.0 \cdot 10^{-2}$ | $< 0.6 \cdot 10^{-2}$ |
| zero point determination | $V_{x,y}$ | $6 \cdot 10^{-4}$ | $1.7 \cdot 10^{-3}$ | $2.3 \cdot 10^{-3}$ | $1.8 \cdot 10^{-3}$ |
| | $V_z$ | $5 \cdot 10^{-4}$ | $2.0 \cdot 10^{-3}$ | $3.1 \cdot 10^{-3}$ | $1.9 \cdot 10^{-3}$ |

**Tab. 4.2:** *Table showing the different contributions to the measuring errors and their estimated size for the three molecular ions measured. Conversion accuracies describes the errors due to the uncertainty in the conversion factor from pixels on the camera of ADC channels (for the z direction) to millimeters. The next set of values give an estimate of the statistical error in determining the exact impact position and time of a single fragment and the last set gives an estimate in the error of the determination of the offsets used to shift the impact positions of the two fragments onto a common zero. This requires only one offset for the difference between the two coordinate systems. I and II denote the first (rectangular) and the second (round) detector. All errors are relative.*

factors and offsets obtained from a calibration as described in the last section. The relative accuracy of the conversion factor from pixels to millimeter is about $5 \cdot 10^{-3}$ ($1\sigma$). The accuracy of the offsets for the transformation from the different coordinate systems one gets due to the different deflections by the magnet are typically of the order of 100 $\mu$m. Since these two uncertainties influence each measured event in the same way they can be treated as systematic uncertainties. There is one statistical uncertainty which is the determination of the center of an individual cluster of pixels on the camera. This center of the cluster can also typically be determined with a resolution of about 200 $\mu$m.

The situation is a bit more complicated for the timing measurement. Here an individual calibration had to be done for each anode strip measuring the conversion factor from ADC channels to picoseconds and the offset. The conversion from ADC channels to relative time differences is done by subtracting the offset for the ADC channel as obtained by the calibration, then converting the channel value to picoseconds and afterwards subtracting the offset for a specific charge state that corresponds to time zero. Velocities are obtained by multiplying the timing value in picoseconds with the square of the ion velocity and dividing by the distance between target and detector. The accuracy of each of these steps influences the total accuracy with which the relative velocities in $z$ direction can be obtained. The accuracy of the ADC value to picosecond conversion is estimated to be about 2%, the offset for the specific channel is known to about 30 ps. Since these values have to be determined individually for every ADC channel these uncertainties broaden the $V$-space distribution. The time zero offset needed to move the measurements for different charge states to a common zero has a typical uncertainty of less than 20 ps. The largest error however comes from the limited time resolution of the detector itself. The average time resolution inferred from single particle impacts amounts to about 60 ps ($1\sigma$) for the rectangular detector and about 100 ps for the round detector. From the laser based study of the imaging detectors one can however conclude that the true resolution for the impact of two particles on the same detector is about 50% larger than the resolution measured with single particle impacts [63].

For two particles hitting two detectors the MCP signal from one detector is used as a stop signal for the ADC channels of the other detector. Here the two errors are the time resolution of the ADC channel and the resolution of the stop signal which is somewhere below the time resolution measured for the ADC channels of the detector the stop signal is taken from. The systematic uncertainty of velocity in $z$ direction is obtained from the uncertainties in the ion velocity and the distance between target and detector. Table 4.2 gives estimates for the relative size of all the errors for the different molecular ions measured in this thesis.

The experimental data obtained is a list of velocities and angles in $V$-space. Histograms can be created from this data showing the $V$-space distribution as a function of the different coordinates. The statistical error on each histogram channel is then given by the square root of the number of entries in the channel.

# 5. Results

In this chapter, experimental results for the molecules $HeH^+$ , $LiH^+$ and $CH^+$ will be presented. The molecules were chosen because they are theoretically well understood. By comparing the measured $V$-space distributions to the ones expected from the theoretical distribution in configuration space one can get insight into the processes happening during the explosion.

## 5.1 $HeH^+$

The experiment on $HeH^+$ was done with a 2.5 MeV $HeH^+$ beam from the high current injector. The beam was injected and stored in the TSR. The vibrational relaxation time of $HeH^+$ is known from other experiments (see section 3.2) and is of the order of a few milliseconds. Because of the short lifetime of vibrationally excited states in the molecule, the beam was only stored for times between 200 ms and one second, and continuously extracted during the whole period. By taking only data of molecules which were stored longer than 100 ms, one could thus be sure to measure vibrationally relaxed molecules.

The measurement was done using a $0.7\,\mu\text{g/cm}^2$ Formvar foil as the Coulomb explosion imaging target. Two groups of experiments were performed: The first possibility (I) was to measure both the Helium and the Hydrogen fragments on the rectangular detector, the other possibility (II) was to measure the Helium fragment on the rectangular detector and the Hydrogen on the round one. For the measurement (II) a magnetic field of about 350 and 520 Gauss was used, depending if one wanted to measure charge $He^+$ or $He^{++}$.The rectangular detector was moved out of axis by 38 mrad for the measurement of $He^+$ and $H^+$ and by 113 mrad for the measurement of the $He^{++} + H^+$ explosion.

At first only events are analyzed that consist of a $He^{++}$ and a $H^+$ measured on either one or two detectors. Figure 5.1 shows a measurement of the explosion of $HeH^+$ into $He^{++}$ and $H^+$ using two detectors. It shows the 2 dimensional density plots of the transverse impact positions of the molecular fragments. The plot on the left shows the Helium ions on the rectangular, the one on the right the Hydrogens on the round detector. As can be seen in these plots, the integration over the measured events gives a ring like structure on the detectors. This structure

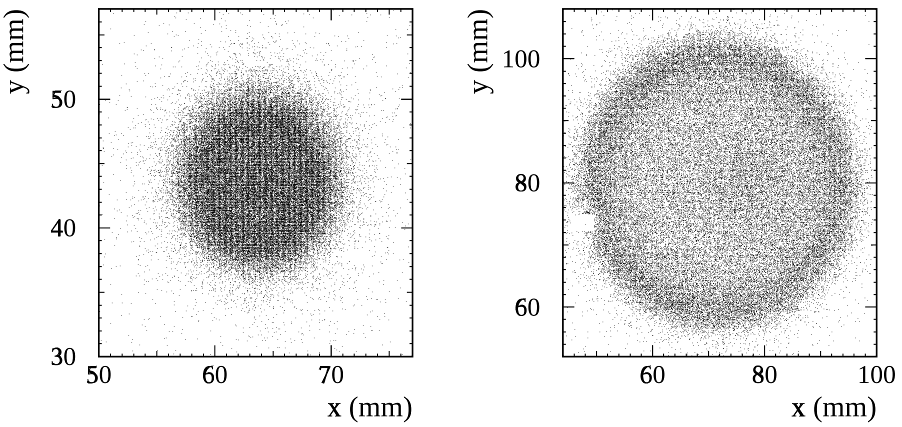

**Fig. 5.1:** *The two figures show the density plots of the transverse impact positions of the molecular fragments* $He^{++}$ *and* $H^{+}$ *on the two detectors. The left plot shows a picture of the first (rectangular) detector with the* $He^{++}$ *ions, the right plot shows the circular detector with the protons.*

can be used to determine the centers of each of the explosion cones as discussed in section 4.6. The small rectangular spot without events in the right plot is because the MCP of this detector had a so called “hot spot” in this region which had to be cut out in the data analysis.

After removing the relative offsets between both rings and converting the detector units to relative velocities as discussed in section 4.6, one gets to a vector of relative velocities $\mathbf{V}= (V_x, V_y, V_z)$ (see section 4.5). Figure 5.2 shows the projection of the $V$-space distribution $P(V_x, V_y, V_z)$ onto the three components $V_{x,y,z}$ of the relative velocity. For an ideal measurement of a molecule with a fixed bond length, this plot should give a box for each of the directions. Because the molecular bond length is not a delta function, the edges of the distributions are smeared out. The distributions in $V_x$ and $V_y$ agree with each other and look quite similar to the smeared box expected from an ideal explosion process. Both curves do however show a peak at $V_i = 0$. This peak can be explained by looking at the plot for $V_z$ which does not show a bump at $V_z = 0$, but an excess of events at large absolute velocities $V_z$. These events with a large relative velocity in $V_z$ can be explained by a wake effect in the target as will be explained in more detail below. Without the contribution from target effects and detector resolutions, the measured $V$-space distribution $P(V)$ should not depend on the angles $\Theta$ and $\Phi$ (see section 4.6). These angles describe the orientation of the molecular fragments in space at the point where they hit the detector, and are related to the molecules orientation during the passage through the foil. Since the resolution of the detector is not perfect and effects from the target might occur, a check of the dependence of $P(V)$ on $\Theta$ and $\Phi$ might help to find influences of these effects onto the measured distribution $P(V)$. In figure 5.3 the corresponding correlations between $P(V)$ and the angles $\Theta$ and $\Phi$ are shown. Both the experimental results as well as the expectation from

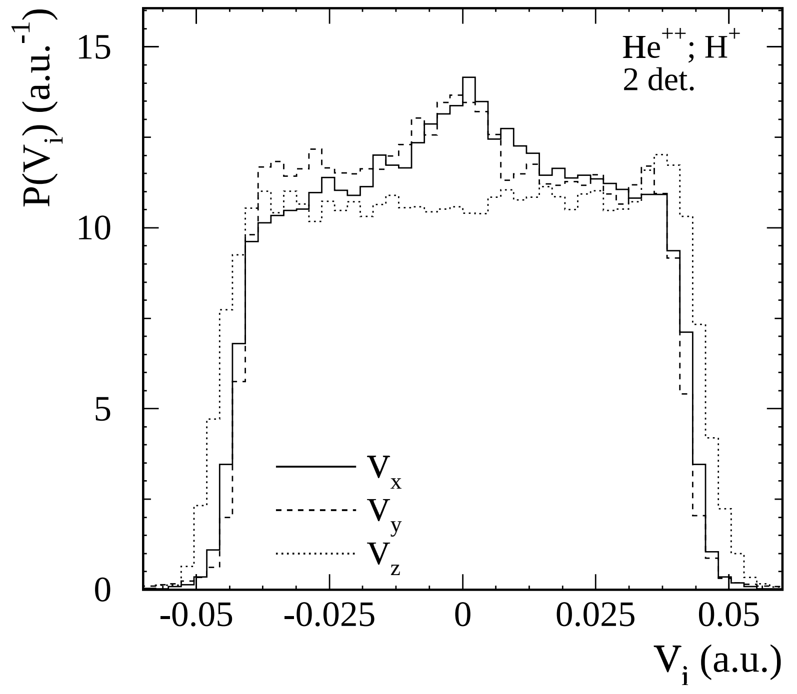

**Fig. 5.2:** *The projection of the v-space distribution $P(\mathbf{V}_{rel})$ onto the three components of the relative velocity $V_{x,y,z}$ between the Helium and the Hydrogen fragments. The x and y components agree well, while the z component is about 10% wider then the x and y components due to the wake effect in the target.*

the simulation are shown. The upper row in the figure shows the dependence of the relative velocity on $\Phi$. As can be seen, the distribution of relative velocities is independent of this angle (there is a small dip in the experimental distribution at $\Phi = 1.9$ which can be explained by the cut that can be seen in the right plot of figure 5.1). The other two plots in figure 5.3 show a plot of $P(V)$ versus $\cos\Theta$ where a clear dependence on the angle is observed in the experimental data. $\cos(\Theta) = \pm 1$ means that the fragments hit the detector with a large time difference, but (if they wouldn't be separated by a magnetic field) at the same point on the detector, while a $\cos(\Theta)$ of 0 means, they arrived at the same time. The influence of errors in the timing measurements to the $V$-space distributions is smaller, the smaller the absolute value of $\cos(\Theta)$. In contrast to the measurement, the simulated data shows only a small broadening for $\cos\Theta = \pm 1$ due to the time resolution which is not as good as the spatial resolution. In the experimental data the limited time resolution can only explain part of the observed effect. Additionally to the smearing by the time resolution, a clear enhancement of the number of events can be seen for $\cos\Theta = \pm 1$ where the enhancement is quite small for $\cos\Theta = -1$ but very large for $\cos\Theta = +1$. At the same time, the mean of the velocity distribution is shifted to

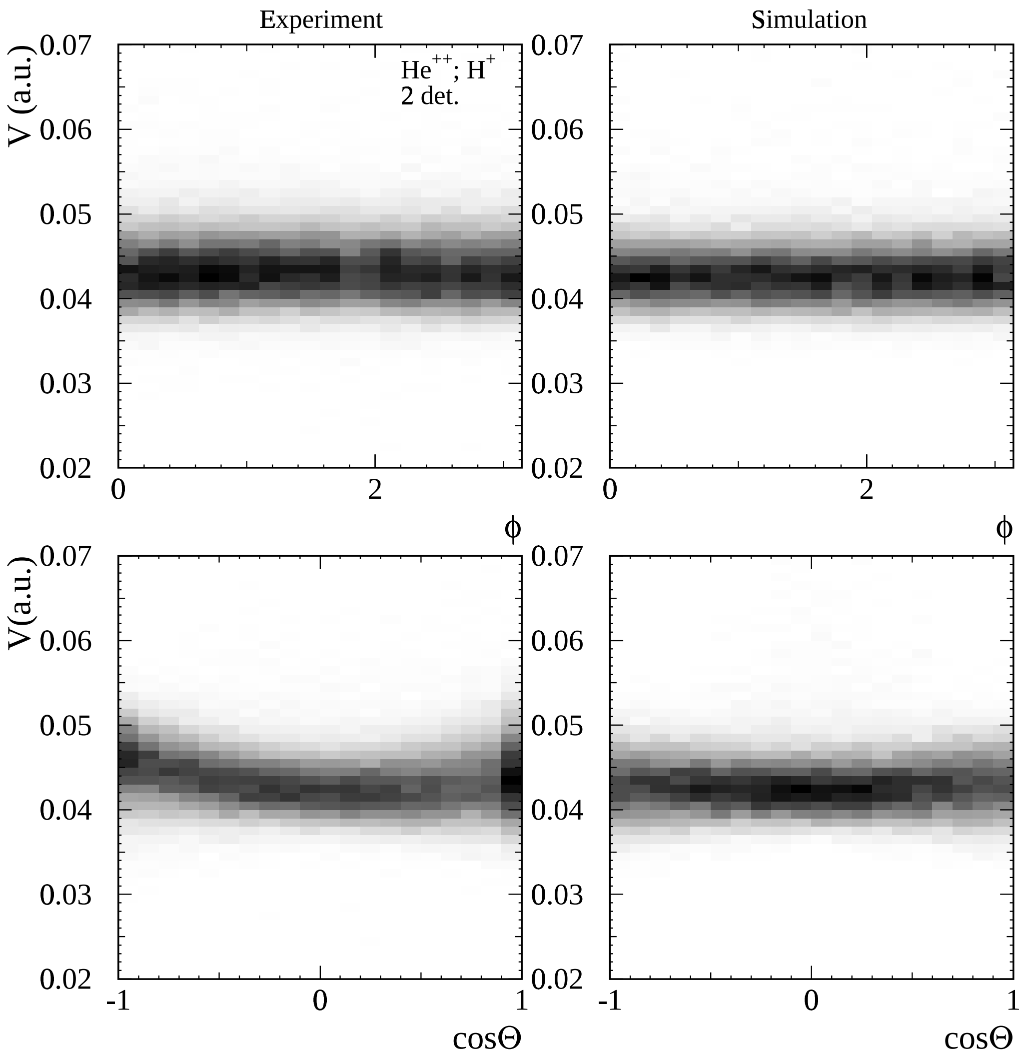

**Fig. 5.3:** *Dependence of the relative velocities between Helium and Hydrogen in the explosion of* $HeH^+$ *into* $He^{++}$ *and* $H^+$ *on the angles* $\Theta$ *and* $\Phi$*. The left plots show the experimental results, while the right plots show the simulation including target effects (except for wake fields) and detector resolution. While there is no dependence on* $\Phi$ *a clear dependence on the angle* $\Theta$ *is observed. The deviation from the simulation that can be seen for* $\Theta = \pm 1$ *is due to the wake effect happening in the target.*

larger relative velocities for these orientations. A possible explanation is a wake effect in the target foil between the Helium and the Hydrogen ion. The Helium as the heavier ion produces a stronger wake field behind it when passing the foil than the Hydrogen. Because the Hydrogen is lighter it also gets influenced much easier from an existing wake field than the Helium. Both effects should add up, so that one expects to see a much larger wake effect when the Hydrogen follows the Helium ($\cos\Theta \approx +1$) than the other way round ($\cos\Theta \approx -1$), as can indeed be seen here. Because the effects of the wake fields are not modeled in the present CEI simulation,

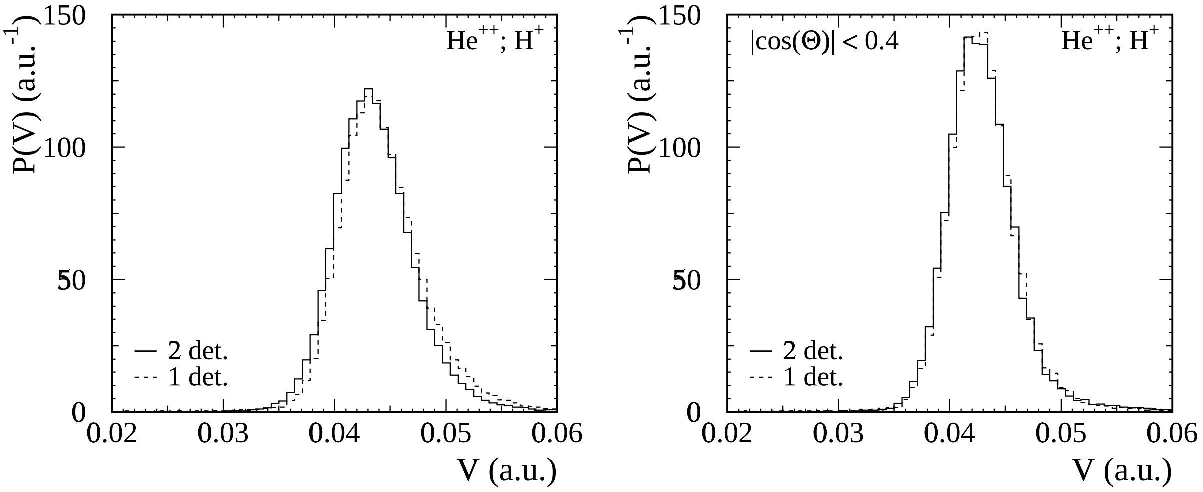

**Fig. 5.4:** *Comparison of the measurements of HeH$^+$ dissociating into He$^{++}$ and H$^+$ on one and two detectors. The solid line shows the measurement where the Helium and the Hydrogen were measured on two different detectors, while the dashed line shows the results when both fragments were detected on one detector. In the left plot one can see the V-space distribution without any cuts, in the right plot a cosine cut of 0.4 was applied.*

these events are removed from the subsequent analysis. In most of the data presented here, a cut of $|\cos\Theta| < 0.4$ has therefore been applied.

Up to now all results shown were from a measurement where each fragment was measured on a separate detector (scheme II). This had the advantage that one does not get crosstalk between two particles hitting the same detector as observed in other experiments [63, 20]. To study the influence of this effect, the same measurement of HeH$^+$ was also done with a setup where both fragments hit the same detector (scheme I). Figure 5.4 compares the measured $V$-space distributions for both cases. The figure on the left shows the distribution of relative velocities without any additional cuts, the figure on the right shows the distribution after applying a cut of $|\cos\Theta| < 0.4$. The left figure shows some differences in the distributions which have to be detector effects and are most probably due to the crosstalk problems one gets when two particles hit different anode strips on the same detector (see [63]). One gets, however, good agreement between the two distributions, if one cuts away the events where the two particles have a large time difference with a cut on $\cos\Theta$. The measurements then do agree almost perfectly. The remaining differences are well within the systematic errors given by the errors in the determination of the beam velocity and the detector geometry.

Figure 5.5 shows the projection of the measured $V$-space distribution onto the cosine of $\Theta$ $P(\cos\Theta)$ for the two measurements. If one assumes, that the molecule is randomly oriented at the entrance of the foil, one expects to see a flat distribution. The observed distributions are

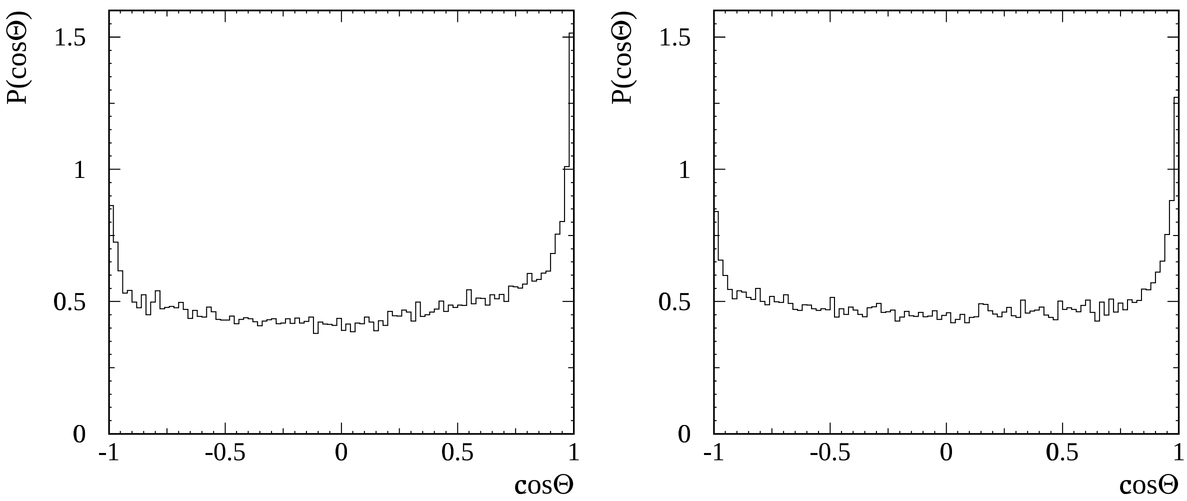

**Fig. 5.5:** *Histograms showing the distribution* $P(\cos\Theta)$ *for* $HeH^+ \rightarrow He^{++} + H^+$. *Left plot shows the result for the measurement of both fragments on one detector, in the right plot the two fragments were measured on different detectors.*

more or less flat for most of the range but deviate strongly at $cos(\Theta) = \pm 1$. The left plot shows the distribution obtained when measuring both fragments on the same detector, while the plot on the right shows the distribution when each fragment was measured on a detector of its own. It can be seen that the distribution for the measurement on two detectors (fig. 5.5 on the right) is evenly distributed in the range (-0.9. . .0.9), while the measurement on one detector (fig. 5.5 on the left) shows some structure in this range. At the same time, the peaks at ±1 are lower for the measurement on two detectors. This suggests that the peaks at ±1 can be explained with a wake effect in the target foil [27, 28], but some of the deviations from a flat distribution seen in the measurement on one detector are due to the detector effects.

To summarize, one can see that the crosstalk[1] does influence the measured distribution $P(V)$, but it could also be shown, that by applying a cut on the angle $\Theta$ most of this influence can be removed. To be on the safe side, the remaining analysis will be done with the data measured on two detectors.

After discussing the measurements for the explosion of $\mathrm{HeH}^+$ into $\mathrm{He}^{++}$ and $\mathrm{H}^+$, and excluding possible systematic errors on the measured distribution $P(V)$ due to detector or target effects, the following discussion will focus on the dependence of $P(V)$ on the final charge state of the Helium. In figure 5.6, one can see the measured $V$-space distributions of $\mathrm{HeH}^+$. The left picture shows the explosion into $\mathrm{He}^+$ and $\mathrm{H}^+$, while the right histogram shows $\mathrm{He}^{++} + \mathrm{H}^+$. In both

---

[1] Most of the crosstalk problems have been solved recently with the introduction of new preamplifiers build up for the CEI detectors.

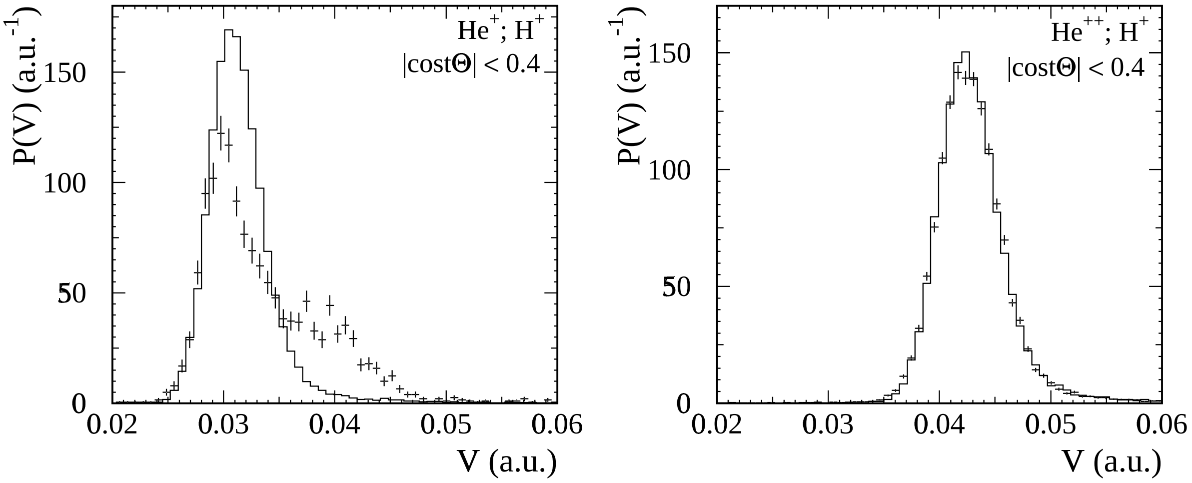

**Fig. 5.6:** *The measured $V$-space distributions of HeH$^+$ into He$^{q+}$ and H$^+$ ($q = 1, 2$) as measured on two detectors at $E_{\mathrm{HeH}^+} = 2\,MeV$ using a Formvar target with a thickness of $0.7\,\mu g/cm^2$, compared to the simple model of the CEI process which assumes point-like charge distributions of the fragments. The points with error bars show the experimental data and its associated statistical error, while the solid line shows the result of the simulation.*

plots a cosine cut of $|\cos\Theta| < 0.4$ was applied, to remove the wake effect. The points with error bars show the experimental results, the solid line shows the theoretical $V$-space distribution one would expect according to the simple Coulomb Explosion model assuming point like charge distributions. The simulations assumed a time resolution of 140 ps (FWHM) for the rectangular detector and 280 ps (FWHM) for the round detector which are the values measured during the calibration of the detector. A target thickness of $0.7\,\mu\mathrm{g/cm}^2$ for the Formvar target was used which is the thickness that has been obtained in a previous measurement [14]. In the right plot it can be seen that the simulation fits the experimental result almost perfectly. This is the expected result, as both the Helium and the Hydrogen are completely stripped and thus point like. For the explosion of HeH$^+$ into He$^+$ and H$^+$, the situation changes completely. The experimental data has a peak at about the position expected by the simulation, but also shows a quite large tail to larger relative velocities.

The reason for this is the remaining electron in the system. To get a correct description of the He$^+$ + H$^+$ channel, one has to calculate all the dissociative potential curves in the HeH$^{++}$ system, calculate transition probabilities from the HeH$^+$ bound state to the different curves and then simulate the explosion process on these curves. First, a comparison of the data to a simple model will be shown while a more complete quantum chemical treatment will follow later. The simple model neglects the influence of the proton on the electron; the electron is only feeling the influence of the Helium core and occupies hydrogen like bound states in the

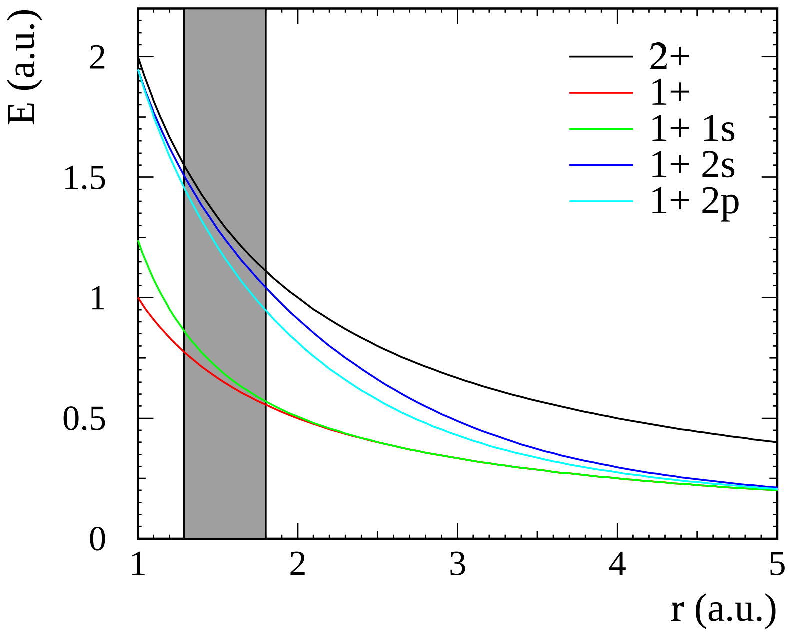

**Fig. 5.7:** *The potential curves between an He$^+$ and an H$^+$ when neglecting the influence of the proton on the last electron in the system. The electron does then occupy hydrogen like states in the He$^+$ atom. The shaded box shows the region where most of the transitions into the dissociative states occur (here given by the region that contains 90% of the R-space distribution of the molecular ground state). The red and black curve are the dissociation curves into the He$^+$/He$^{++}$ + H$^+$ final states according to the Coulomb model, the other curves show the potential surfaces into the He$^+$ +H$^+$ final state assuming the electron is in the 1s, 2s or 2p state of the Helium ion.*

potential of the core. Under these assumptions, the wave function of the electron is known, and given by the bound states of the Coulomb problem. With the help of these wave functions, effective potentials between the He$^+$ atom and the proton can be calculated for each state the electron can occupy in the Helium atom. The resulting potentials are plotted in figure 5.7 together with the Coulomb curves. The bond length of the HeH$^+$ molecule is about 1.5 a.u. and the foil induces a vertical transition to the plotted dissociative curves at this distance. The Franck-Condon region where most vertical transition occur (90% of the transitions from the molecular ground state occur here) is shown in grey in figure 5.7. If the electron is in the 1s state, the resulting potential in the Franck-Condon region is similar to the pure Coulomb like potential used in the simulation shown above. This explains, why the peaks of the pure Coulomb model and the experimental data shown in fig. 5.6 are at about the same relative velocity. The potential curves where the electron is in a 2s or 2p state are already quite different from the pure Coulomb curve and are almost up to the Coulomb curve of the naked Helium at a distance of 1.5 a.u. The reason is that the average distance of the electron from the Helium nucleus is

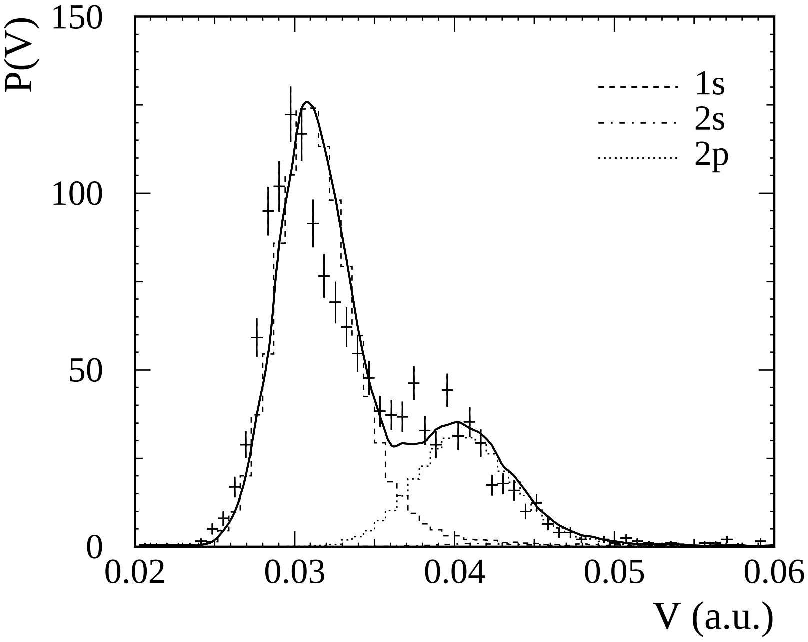

**Fig. 5.8:** *The measured V-space distributions of HeH$^+$ → He$^+$ + H$^+$, fitted to the three simplified model assigning the remaining electron to different hydrogen-like states of the Helium. The fit shows that according to this model for about 75% of the explosions the electron is in the ground state of the Helium ion.*

larger than the bond length of the HeH$^+$. According to this model, the explosion process can now take place via a series of different paths, namely via all possible states the electron can occupy in the Helium atom.

As one can see in figure 5.8, the agreement is better, but still considerable deviations between theory and experiment remain. According to this model, almost all of the explosion goes via two paths, leading to two different final states: One where the He$^+$ is in the ground state, the other path leads to a He$^+$ where the electron is sitting in a 2p state after the explosion. The other curves (into the 2s final state or the states with the electron sitting in the M shell after the explosion), lead to $V$-space distributions with even larger relative velocities and do not seem to be populated according to the fit.

To get a more quantitative description of the explosion, a quantum chemical calculation of the potential curves of HeH$^{++}$, using the Relativistic Local Density Approximation (RLDA), performed by T. Jacob and S. Fritzsche [64], was used. The dissociative potential curves as calculated by them are shown in figure 5.9. All curves were normalized to zero at infinity, to be able to directly compare the curves. It is obvious that the curves have some features in common with the simple model presented earlier, but deviate considerably in the details. Most prominently, the energy of the curve leading to the final state He$^+$(1s) + H$^+$ is below the

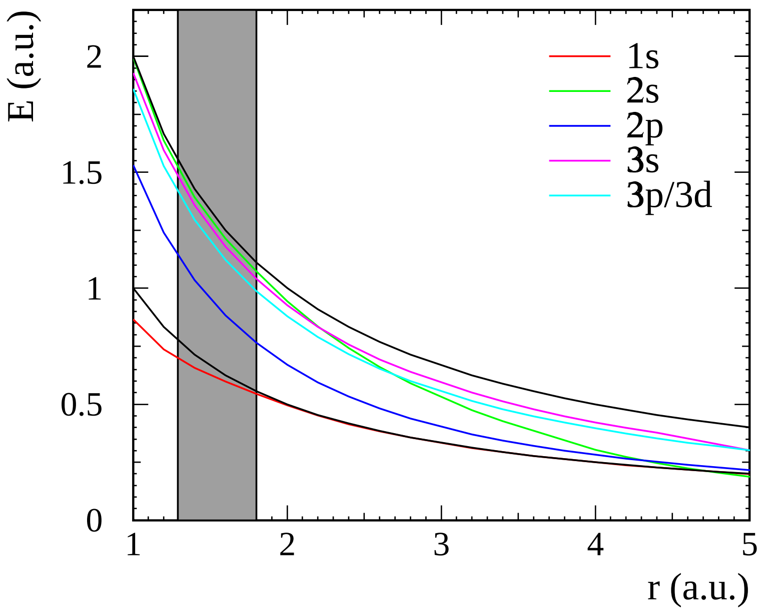

**Fig. 5.9:** *The potential curves between an He$^+$ and an H$^+$ from a full quantum chemical calculation [64]. The curves are labeled according to the final state of the He$^+$ atom. The curves going to the 3p and 3d final states are indistinguishable on this scale and thus plotted together. The Coulomb curves are shown in black for comparison.*

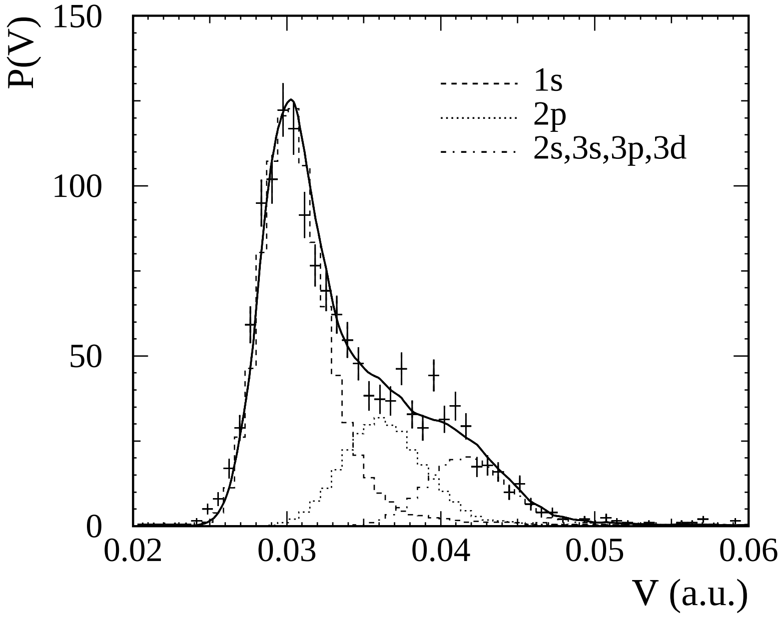

**Fig. 5.10:** *The measured V-space distributions of HeH$^+$ →He$^+$ + H$^+$, fitted to the V-space distributions obtained using the calculated potentials shown in fig. 5.9. The solid line is the fit, the dashed line the contribution form the 1s curve (64%), the dotted line the contribution from the 2p curve (22%) and the slash-dotted line is the sum of the contributions from 2s, 3s, 3p and 3d curves (14%).*

pure Coulomb curve, so in this case the electron gives rise to some binding effects. The second difference is the curve leading to the He$^+$(2p) + H$^+$ final state which is also significantly lower than in the simple model. The curve leading to the He$^+$(2s) + H$^+$ final state deviates from the model at larger distances, but agrees with the model at the distance of 1.5 a.u. where the explosion starts. Since the explosion process is only sensitive to the total energy released, the shape and energy of the dissociative curve in the Franck-Condon region of the HeH$^+$ molecule influences the explosion process, while the shape at larger distances is mostly insignificant.

The curves leading to the final states He$^+$(2s), He$^+$(3s), He$^+$(3p) and He$^+$(3d) look mostly the same at the bond length of the HeH$^+$ molecule and thus lead to almost indistinguishable $V$-space distributions; they were in the following fit of the data represented by a single distribution, obtained by averaging over all the corresponding $V$-space distributions. Using this distribution together with those expected for He$^+$(1s) + H$^+$ and He$^+$(2p) + H$^+$ the measured $V$-space distribution $P(V)$ was fitted (figure 5.10). The fit shows good agreement with the experimental data. Additionally, the fit parameters give some information about the final state distribution of the He$^+$ atom after the Coulomb Explosion, as they represent the transition probabilities into the different dissociative states of the HeH$^{++}$ molecule induced by the target foil. According to the fit, 64% ± 2% of the dissociating molecules go into the He$^+$(1s) final state, 22% ± 2% into the 2p final state and 14% ± 2% go into the other (2s, 3s, 3p, 3d and higher) final states.

While the explosion of HeH$^+$ into He$^{2+}$ and H$^+$ can be understood very well with a simple Coulomb like model, the measured $V$-space distribution $P(V)$ for the charge state 1+ of the Helium cannot be explained in this picture. For the latter channel a better description is given by a model with a proton sitting in the unperturbed potential of a He$^+$ atom. However, to get a full understanding of the process happening, a quantum chemical calculation of the dissociative potential curves of the HeH$^{++}$ pseudo molecule had to be used.

## 5.2 LiH$^+$

LiH$^+$ is the next heavier XH$^+$ molecule after HeH$^+$ and should show similar effects as HeH$^+$. However, its bond length and binding energy is very different from HeH$^+$ (see chapter 3) and might therefore lead to different effects in the measured $V$-space distribution. The CEI measurement was performed using a 0.7 $\mu$g/cm$^2$ Formvar target. The beam energy used in the experiment was 6.5 MeV and the beam was stored for up to two seconds in the TSR and continuously extracted during this time. The Lithium and the proton were measured on the same detector but as shown for the measurement of HeH$^+$ $\rightarrow$He$^{++}$ + H$^+$ the crosstalk between the different anode strips on the detector should not influence the measured $V$-space distribution if one applies a reasonable cut in $\Theta$.

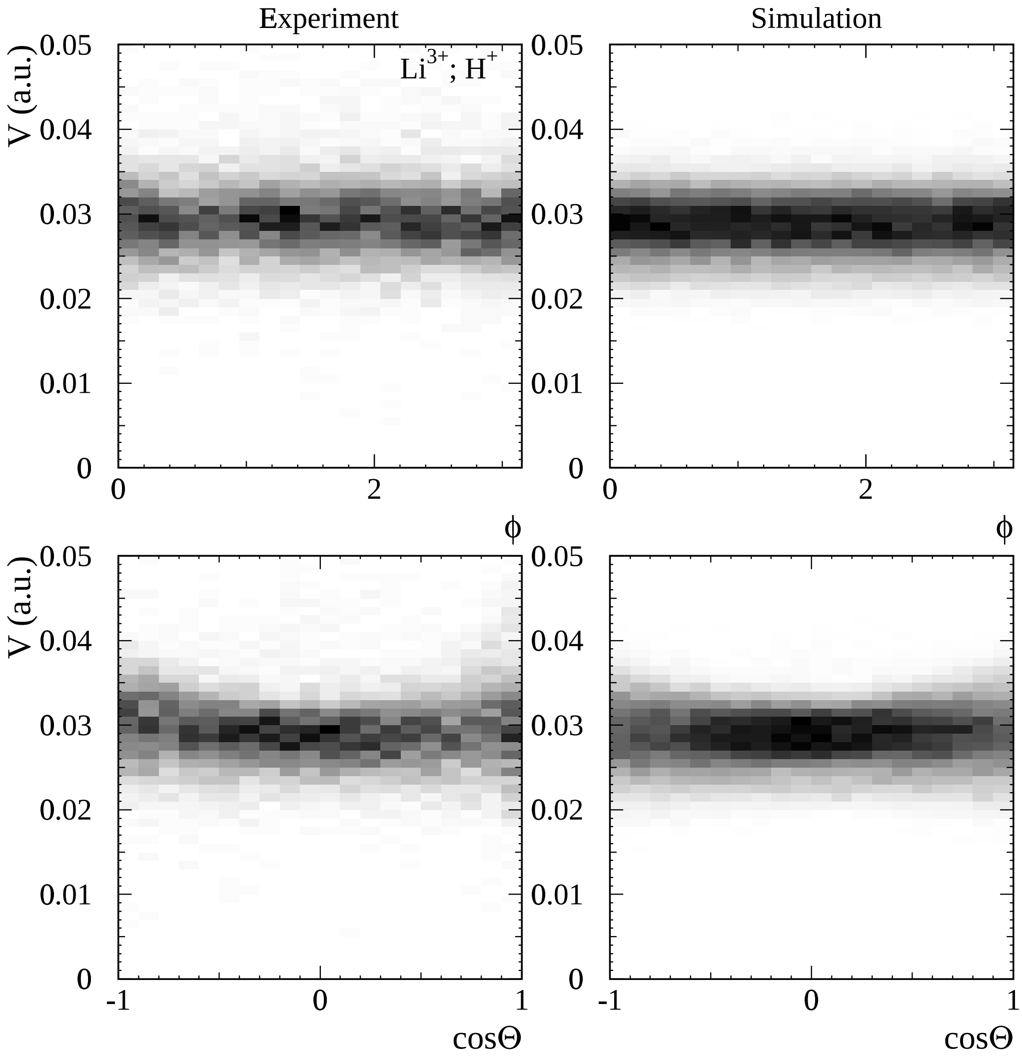

**Fig. 5.11:** *The dependence of $P(V)$ of the LiH$^+$ molecule dissociating into the Li$^{3+}$ and H$^+$ on the angles $\Theta$ and $\Phi$. Both fragments were measured on the same detector. The $V$-space distribution shows no $\Phi$ dependence and a smaller $\Theta$ dependence than the measured distribution of $HeH$. The left plots display the measurement, the right plots are the result of the simulation.*

Similar to the HeH$^+$ analysis the Coulomb explosion into the naked ions Li$^{3+}$ and H$^+$ will be discussed first before the lower charge state channels are described. Figure 5.11 shows the measured angular dependence of the $V$-space distribution $P(V)$ of the LiH$^+$ molecule dissociating into a naked Lithium and a proton. As in the case of HeH$^+$ no dependence on the $\Phi$ angle can be seen. The dependence on $\cos\Theta$ is much less pronounced than for the HeH$^+$ molecule. The main reason for this is probably the much larger bond length of the molecule, which leads to a reduced wake effect between the two fragments as can be seen in figure 5.12. The broadening of the $V$-space distribution for large absolute values of $\cos\Theta$ can

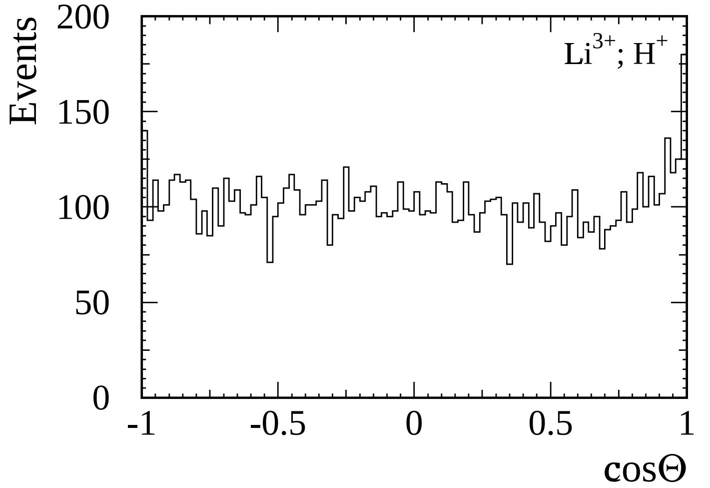

**Fig. 5.12:** *The distribution of $V$-space events as a function of the angle $\Theta$. A small wake effect can be seen for $\Theta = +1$, but its size is small compared to the effect observed in HeH$^+$.*

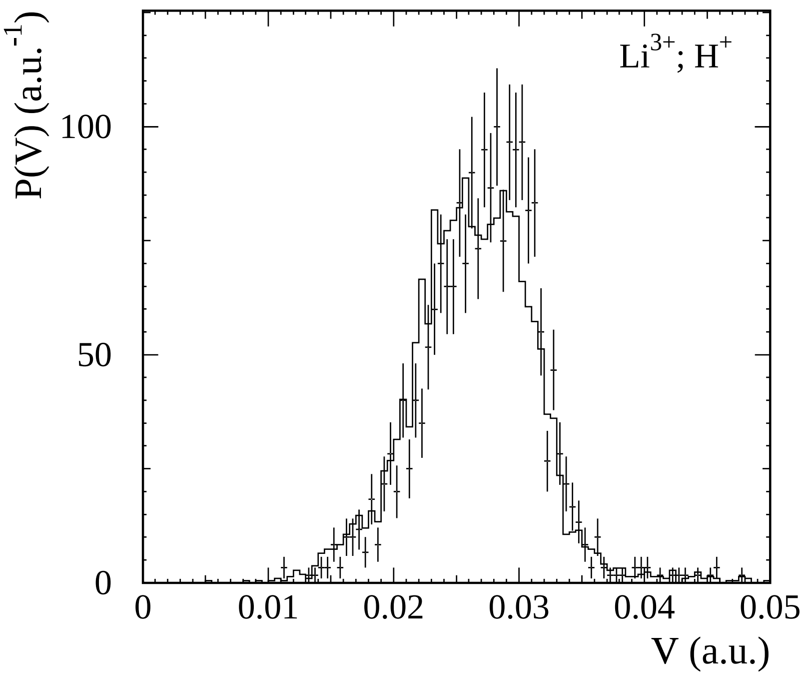

**Fig. 5.13:** *The $V$-space distribution of LiH$^+$ exploding into naked Lithium and a proton for different storage times. The line shows the measured distribution for storage times shorter than 500 ms, the histogram with error bars the distribution for storage times larger than 1300 ms. The distribution for long storage times is a bit higher at $V \approx 0.03$ and a bit lower at the left edge of the distribution which might indicate some cooling, the change is however not statistically significant.*

be attributed to the time resolution of the detector as can be seen by comparing to the result of the simulation. The results of the simulation shown in figure 5.11 were obtained by using a distribution in $R$-space which assumed an initial distribution of vibrational states equal to the values obtained further below. To reduce the influence of the time resolution on the $V$-space distribution and to avoid wake field effects a cut of $|\cos\Theta| < 0.4$ has been applied as in the case of HeH$^+$.

The lifetimes of the vibrational states of LiH$^+$ were estimated to be of the order of several seconds, longer than the two seconds for which the molecular beam was stored and extracted.

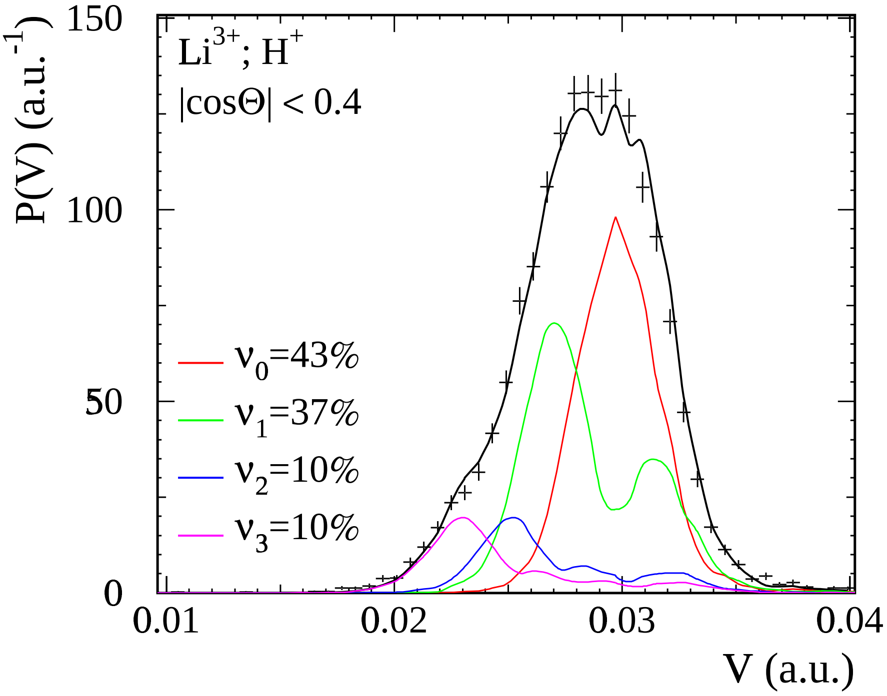

**Fig. 5.14:** *The $V$-space distribution for LiH$^+$ $\rightarrow$Li$^{3+}$ + H$^+$ measured for storage times between 500 ms and 2 seconds and the vibrational distribution fitted to it. Around 43% ± 1% of the molecules are in the vibrational ground state, 37% ± 2% in $\nu = 1$ and around 10% ± 1% in in each of $\nu = 2$ and $\nu = 3$. The last two vibrational states $\nu = 4, 5$ are unpopulated according to the fit, likely due to field ionisation of these highly excited molecules in the dipole magnets of the storage ring.*

As there are no measurements for longer storage times these two seconds are the only time interval in which one can try to observe internal cooling of the molecule. Figure 5.13 shows the measured $V$-space distribution for LiH$^+$ for short ($< 500$ ms) and long ($> 1300$ ms) storage times. Within the statistical errors, no cooling is observed even though the difference between the measured distributions indicates a shift into the right direction. This leads to the conclusion that the lifetimes of the vibrational states are somewhat longer than two seconds in agreement with the theoretical prediction (see section 3.3).

Since there are no electrons left in the dissociating molecule, the explosion can be expected to follow a pure Coulomb like model and the simulation should give a good description of the explosion process. This allows the extraction of the relative population of the different vibrational states in the molecule which can be done by a procedure similar to the one used for the measurement of the vibrational lifetimes of HD$^+$ (see [12]). For each of the different vibrational states a simulation was performed, to obtain the $V$-space distributions one would get if all the molecules would occupy a single vibrational state. The measured distribution was then fitted to a sum of these $V$-spaced distributions for single vibrational states with the relative populations of each state as fit parameters. The result of the fit is shown in figure 5.14 and gives directly the vibrational population of the molecule. Only about 43% of the molecules are in the vibrational ground state as opposed to about 80% that would be expected in thermal equilibrium. But as noted in section 3.3 the lifetimes of the vibrational states are of the order of seconds, so a cooling to thermal equilibrium could not be expected. The fit shows that all vibrational states up to $\nu = 3$ still exist in the measured ion beam after a storage time of more than 500 ms. It is however interesting to notice that the last two vibrational states $\nu = 4$ and $\nu = 5$ do not seem to be populated. The fit gives an upper bound of 0.5% for the population of $\nu = 4$ and of 0.2% for the $\nu = 5$ state. One possible reason could be the field ionisation expected to occur in the dipole magnets of the ring. A corresponding estimate shows that the LiH$^+$ ions see an electric field of about $E = 1.4 \cdot 10^7\,\mathrm{V/m}$ in their rest frame while flying through the dipoles. This electric field modifies the binding potential between the Lithium and the Hydrogen. It has been shown (see ref. [65]) that the potential which has to be added to the molecules binding potential is given by $-ReE\mu/m_{Li}$ where $R$ is the intra nuclear distance and $\mu$ the reduced mass of the molecule. For LiH$^+$ , this results in a decrease of the dissociation limit by $2.2 \cdot 10^{-3}\,\mathrm{eV}$. As the $\nu = 4$ state has a binding energy of $6 \cdot 10^{-3}\,\mathrm{eV}$ it should still be stable against field ionisation, while the $\nu = 5$ state with its binding energy of $1.2 \cdot 10^{-3}\,\mathrm{eV}$ could dissociate. This estimate can thus explain, why no LiH$^+$ in $\nu = 5$ is observed in the stored ion beam. As the model used above is quite simple, it can, however, not be excluded that the $\nu = 4$ state get field ionized aswell.

Now the measurements of the other charge states will be presented and compared to the results of the simulation using the Coulomb model. The vibrational population has to be the same for all the charge channels measured, so the lower charge channels should also be represented by these distributions, if the explosion does indeed proceed on Coulomb trajectories. Figure 5.15 shows that the distributions for the explosions into the other charge state channels agree quite well with the expectation for low relative velocities, but deviate at high relative velocities. This is similar to what has been seen in the HeH$^+$ data, but the size of the effect is significantly smaller. This is understandable, because of the large bond length of the LiH$^+$ molecule. In the simple model presented during the analysis of HeH$^+$ , the deviations from the Coulomb curve are due to the finite size of the electron cloud around the Helium atom. In the case of Li$^{2+}$, the remaining electron is bound even tighter than for He$^+$ and thus one expects the explosion to follow a pure Coulomb like curve in case the electron is in the K or L shell. Only for $n = 3$ or higher where the mean distance of the electron from the nuclei is 3 a.u. or more, a deviation from the pure Coulomb case can be expected. Looking at the difference between the simulated and the measured distribution gives that about $6\% \pm 1\%$ of the exploding molecules follow a

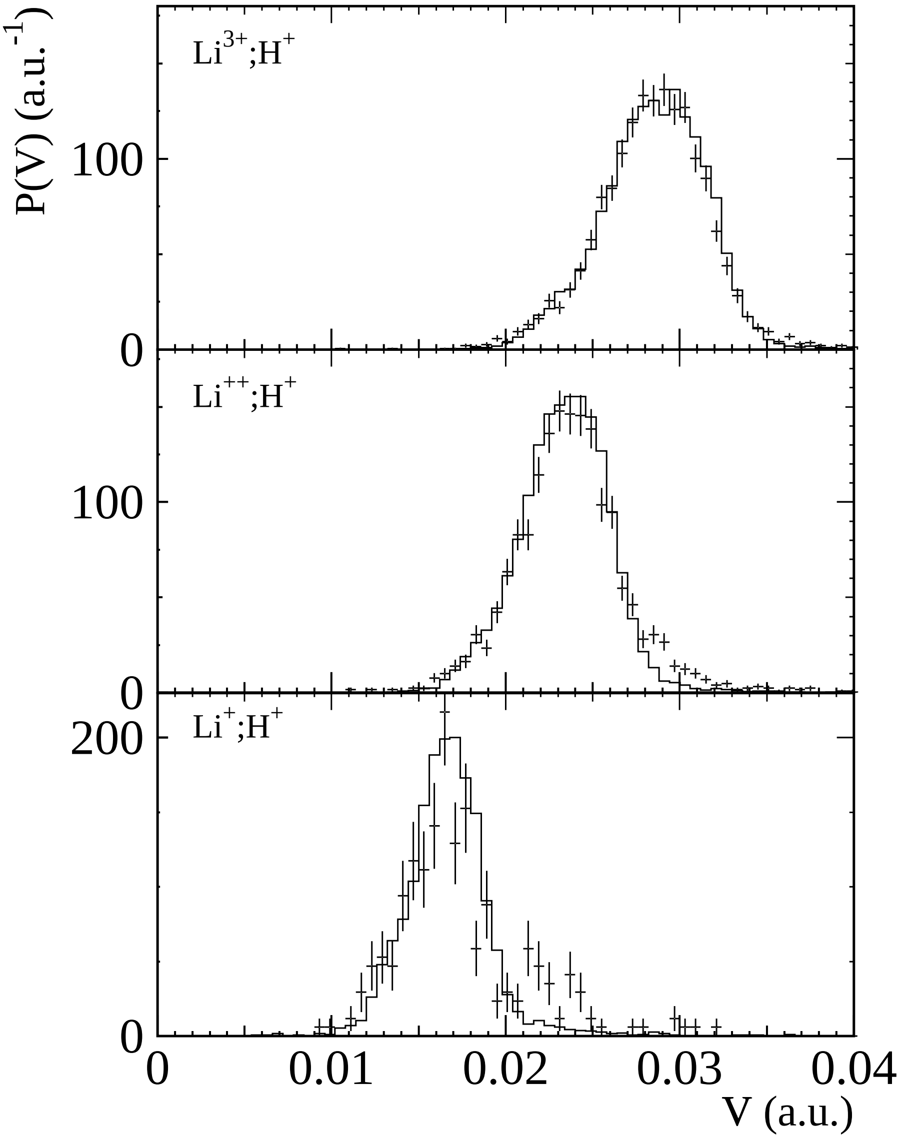

**Fig. 5.15:** *The measured V-space distributions for the three charge states of LiH$^+$ compared with simulated V-space distribution obtained from the fitted distribution of vibrational states.*

path which is not Coulomb like. Doing the same analysis for the Li$^+$, shows that in this case about 13% ± 3% of the molecules followed a non Coulomb like path during explosion.

This shows that also in the case of LiH$^+$, which has a much larger bond length than the HeH$^+$ molecule, the simple picture of an explosion of point like ions cannot fully describe the explosion process. The deviations are, however, small and most of the explosion channels proceed via potential curves that are very close to the Coulomb curves.

## 5.3 $CH^+$

The $CH^+$ measurements were done during a beamtime in November 1999. Due to a leak in the electron cooler of the storage ring at that time, the vacuum in the storage ring was an order of magnitude worse than usually. This resulted in a drastically reduced beam lifetime of only about 750 ms for the $CH^+$ beam making it impossible to measure at storage times longer than two seconds. As the slowest vibrational transition in $CH^+$ is about 700 ms, one can not expect to get internal cooling to thermal equilibrium. In addition a fraction of the molecules will remain in the metastable electronic state (see section 3.4). The influence of the internal excitation on the measurement will be discussed below.

The Coulomb explosion was measured at two different beam energies (6.5 and 4 MeV). Changing the beam energy influences the size of the explosion cones on the detector, but the main change is in the better resolution in the $z$ coordinate for lower energies since the time difference between two fragments is inversely proportional to the beam energy. On the other hand, the scattering in the target foil increases for lower energies. The change of the $V$-space distribution $P(V)$ is however expected to be small because of the thin DLC target ($0.5\,\mu g/cm^2$) used in this experiment. To cross-check target effects, the 6.5 MeV beam of $CH^+$ has been measured with two targets: the thin DLC target of about $0.5\,\mu g/cm^2$ and a thicker target of about $1.1\,\mu g/cm^2$. All data shown here was measured on two detectors to exclude effects due to the crosstalk between different anode strips.

The most abundant dissociation channel in the measurements at 6.5 MeV is the explosion into $C^{4+}$ and $H^+$. At 4 MeV the branching ratios into $C^{3+} + H^+$ and $C^{4+} + H^+$ are almost the same, $C^{3+} + H^+$ being a bit more likely. A list of the branching ratios into the different charge states is given in table 5.3.

As in the other measurements, the centers of the individual rings were moved to a common zero and the components of the relative distance between the two fragments has been converted to relative velocities. A check of the dependence of the $V$-space distribution $P(V)$ on the angles can be seen in figure 5.16 at the example of the explosion into $C^{4+}$ and $H^+$. The left column

| Charge state $q$ of Carbon | 2 | 3 | 4 | 5 |
|---|---|---|---|---|
| 4 MeV, thin target | 6.5% | 50.3% | 41.0% | 2.1% |
| 6.5 MeV, thin target | 3.6% | 31.0% | 55.8% | 9.6% |

**Tab. 5.1:** *Branching ratios for the dissociation of $CH^+$ into $C^{q+}$ and $H^+$ with the thin target ($0.5\,\mu g/cm^2$) at 6.5 MeV and 4 MeV. The charge states $C^+$ and $C^{6+}$ could not be observed in the measurements. For the thick target at 6.5 MeV a ratio of 1 to 3.7 between charge states 5 and 4 was observed.*

shows the measurement at 6.5 MeV while the right column shows the same plots for 4 MeV. As for the other cases no dependence on the angle $\Phi$ could be observed. The dependence on $\cos\Theta$ shows the typical broadening for $\cos\Theta \to \pm 1$ which can be mostly explained by time resolution. It can be seen, that the broadening gets smaller for the 4 MeV measurement as would be expected due to the improved time resolution at lower energy. The average velocity shows a small shift towards higher relative velocities and a peak at $\cos\Theta \approx +1$ due to the wake effect. It can also be seen that the wake effect gets stronger at 4 MeV. Figure 5.17 shows this even clearer. While the distribution at 6.5 MeV is almost flat in the region $-0.9 < \cos\Theta < 0.9$ it shows some structure for the 4 MeV measurement. At the same time the peaks of the wake at $\cos\Theta = \pm 1$ are more pronounced in the 4 MeV measurement. In the following a cut of $|\cos\Theta| > 0.4$ is applied to remove the wake effect and reduce the influence of the time resolution.

As was already noted above the storage time of two seconds is not long enough to be able to measure fully relaxed molecules. Figure 5.18 show the difference in the measured distribution

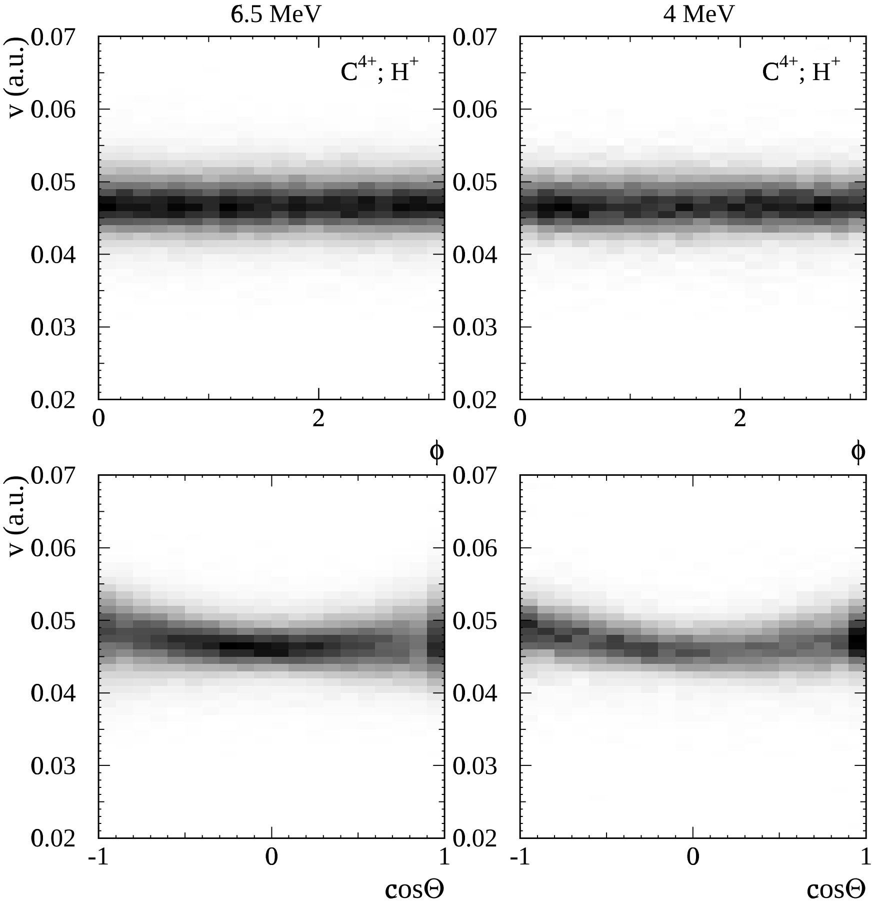

**Fig. 5.16:** *The dependence of the measured distribution $P(V)$ on the angles $\Theta$ and $\Phi$ for the explosion of $CH^+$ into $C^{4+}$ and $H^+$ measured at 6.5 and 4 MeV with a DLC target of 0.5 $\mu g/cm^2$.*

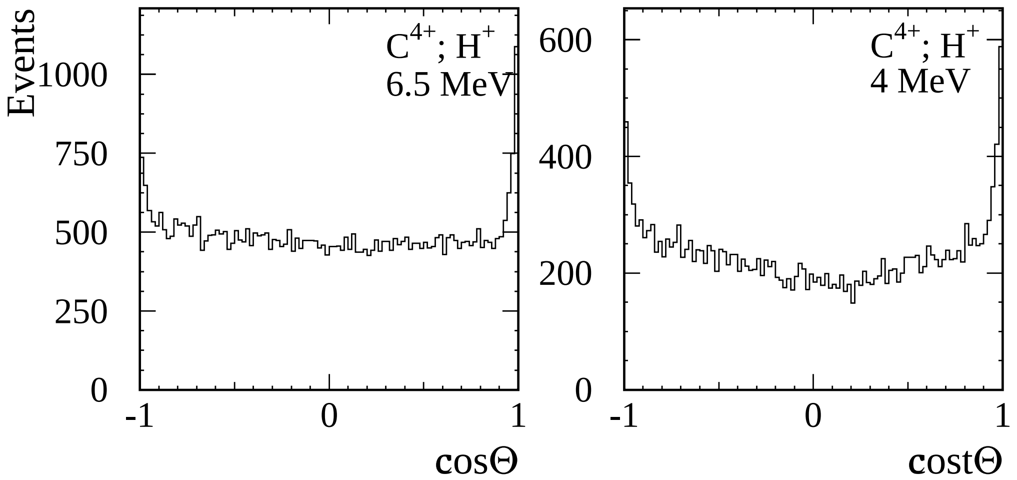

**Fig. 5.17:** *The dependence of the number of measured events in the Coulomb explosion of CH$^+$ into C$^{4+}$ and H$^+$ on $\cos\Theta$ using the DLC target of 0.5 mug/cm$^2$. While the distribution for 6.5 MeV is almost flat in the range $-0.9 < \cos\Theta < 0.9$ some structure can be seen at 4 MeV. At the same time the wake effect at $\cos\Theta = +1$ is stronger for the measurement at 4 MeV.*

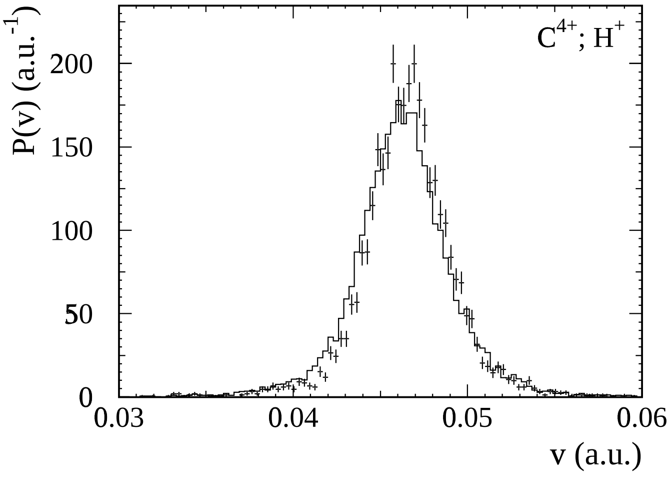

**Fig. 5.18:** *Comparison of the distribution $P(V)$ measured at short storage times ($<$ 500 ms; histogram) and at long storage times (between 1000 ms and 2000 ms; crosses). Cooling of the internal excitations can be observed but the size of the effect is rather small.*

$P(V)$ for storage times shorter than 500 ms compared to times longer than 1 second. While the change is small, it is still significant and is caused by the vibrational relaxation of the molecules. It is interesting to note, that the distribution measured at long storage times is not only more narrow ($2.6 \cdot 10^{-3}$ a.u. versus $2.9 \cdot 10^{-3}$ a.u.) but also that the mean of the distribution is shifted to larger relative velocities. The excited vibrational states of CH$^+$ have a lifetime in the order of half a second (see section 3.4). Because the $X^1\Sigma^+$ potential of the CH$^+$ ground state is quite

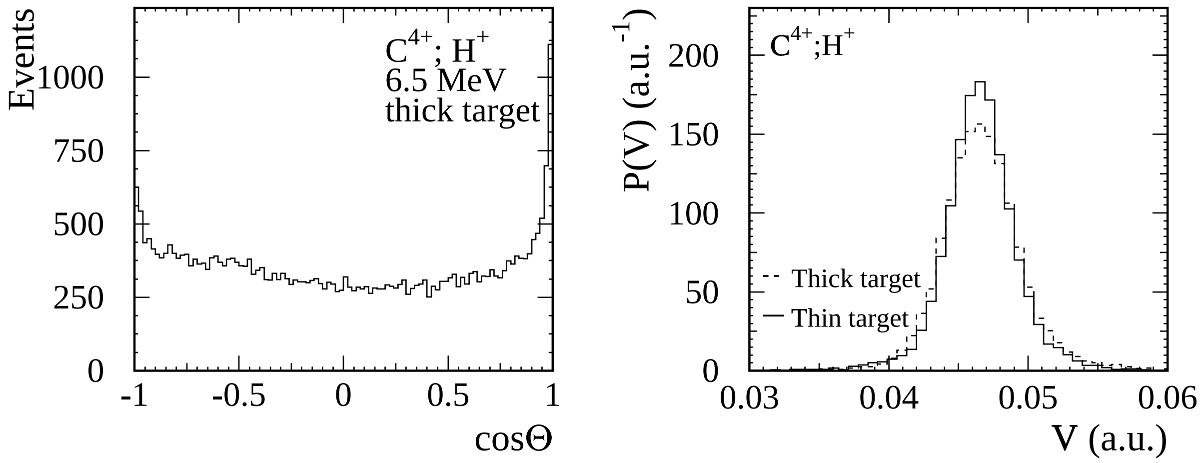

**Fig. 5.19:** *The* $\cos\Theta$ *distribution Comparison of the measurements of* $CH^+$ *into* $C^{4+}$ *and* $H^+$ *with a thin (0.5* $\mu g/cm^2$*) and a thick (1.1* $\mu g/cm^2$*) DLC target.*

anharmonic, the average bond length

$$\langle R\rangle = \int |\Psi(R)|^2 \mathrm{d}R$$

of excited vibrational states in the molecule is quite different from that of the ground state. While the expectation value for the $\langle R\rangle$ is 1.148 Å for the ground state, it is 1.184 Å for the first vibrationally excited state and 1.224 Å for the second excited state [53]. This means, that the average bond length increases by about 3% from one vibrational state to the next, resulting in a decrease of 1.5% in the average relative velocity between the fragments. The metastable $a^3\Pi$ state behaves similarly. A larger average bond length in $R$-space transforms to a smaller average relative velocity in $V$-space. This matches the behavior observed for short storage times, where higher vibrational states are still expected to be populated. A closer examination shows that the largest changes in $P(V)$ occur in the first few hundred milliseconds in agreement with the expected lifetimes of the excited vibrational states in $CH^+$ [54]. Thus all events with a storage time of less than 500 ms were removed from the subsequent analysis.

With the 6.5 MeV beam two measurements with different targets were performed. This allows to study the influence of the Coulomb explosion target on the measured data. For the thick target only data where the Carbon is in charge state 4+ and 5+ is available. The first thing to notice is the branching ratio between charge states 4 and 5. For the thin target ratio is 5.8 to 1 while it is only 3.7 to 1 for the thicker target (see table 5.3). This shows that the first target is so thin that the charge state distribution for the Carbon ions after the foil is still far from equilibrium for the thin target. The simulation predicts a ratio of about 4 to 1 for the equilibrium distribution so the equilibrium charge state distribution seems to be mostly reached for the thick target. The influence of the target thickness on the wake effect can be seen in figure 5.19 on the left. One can see that the thickness of the target has a huge influence on the size of the wake effect. The peak at $\cos\Theta = +1$ is much larger than for the thin target (see figure 5.17), and the shape of the distribution at intermediate angles is not flat anymore.

The plot in figure 5.19 on the right compares the measured distributions $P(V)$ for the charge states $C^{4+}$ between thin and thick targets. A cut of $|\cos\Theta| < 0.4$ has been applied to the data. The result shows only a small additional broadening due to the increased multiple scattering in the thick target. A similar picture can be observed for the explosion into $C^{5+}$ and $H^+$. This shows that the increased target thickness does change the measured $V$-space distribution only slightly due to increased multiple scattering but results in a larger wake effect. On the other hand it produces higher average charge states which might be an advantage for some measurements where the high charge state is needed.

The complete set of different measured charge states at 6.5 MeV with the thin target can be found in figure 5.20. The expectation from a simulated Coulomb explosion of the ground state of $CH^+$ (using the experimentally determined values for beam energy, target thickness and detector resolution) is added for comparison. The charge states 4+ and 5+ do almost fit the model. For the explosion into $C^{5+}$ and $H^+$ the mean of the simulated distribution is shifted by 0.7% to larger relative velocities than the experiment. At the same time the experimental distribution is about 10% wider than the result obtained from the simulation. As the target is extremely thin, shielding effects inside the target foil can not explain this shift. This could be confirmed by simulations that showed that the distribution $P(V)$ is not changed within the experimental resolution by changing the interaction potential between the fragments inside the target foil. As $C^{6+}$ could not be observed in the experiment one can assume that the last electron in the system is too deeply bound to get ionized or excited and is therefore still in the 1s state after the $C^{5+}$ fragments leave the foil. This state is so tightly bound that the Hydrogen sees a point like carbon ion. This excludes binding effects between the Carbon and the Hydrogen due to the remaining electron and the explosion should be governed in a good approximation by a Coulomb trajectory.

The remaining explanation is the vibrational excitation in the system. Since the longest vibrational lifetimes in the $CH^+$ molecule are about 700 ms and higher excited vibrational states should have a significantly shorter lifetime it can be expected that after 500 ms only the lowest three vibrational states (in the two electronic states) are populated. Since the vibrational states of the $a^3\Pi$ state have a slightly larger bond length (leading to smaller relative velocities in $V$-space) and according to [10] more than 50% of the molecules are in this electronic state its first three vibrational states were used to fit the distribution $P(V)$ measured in the explosion into $C^{5+}$ and $H^+$. Fitting both the states of the $a^3\Pi$ and the $X^1\Sigma^+$ curves was not possible

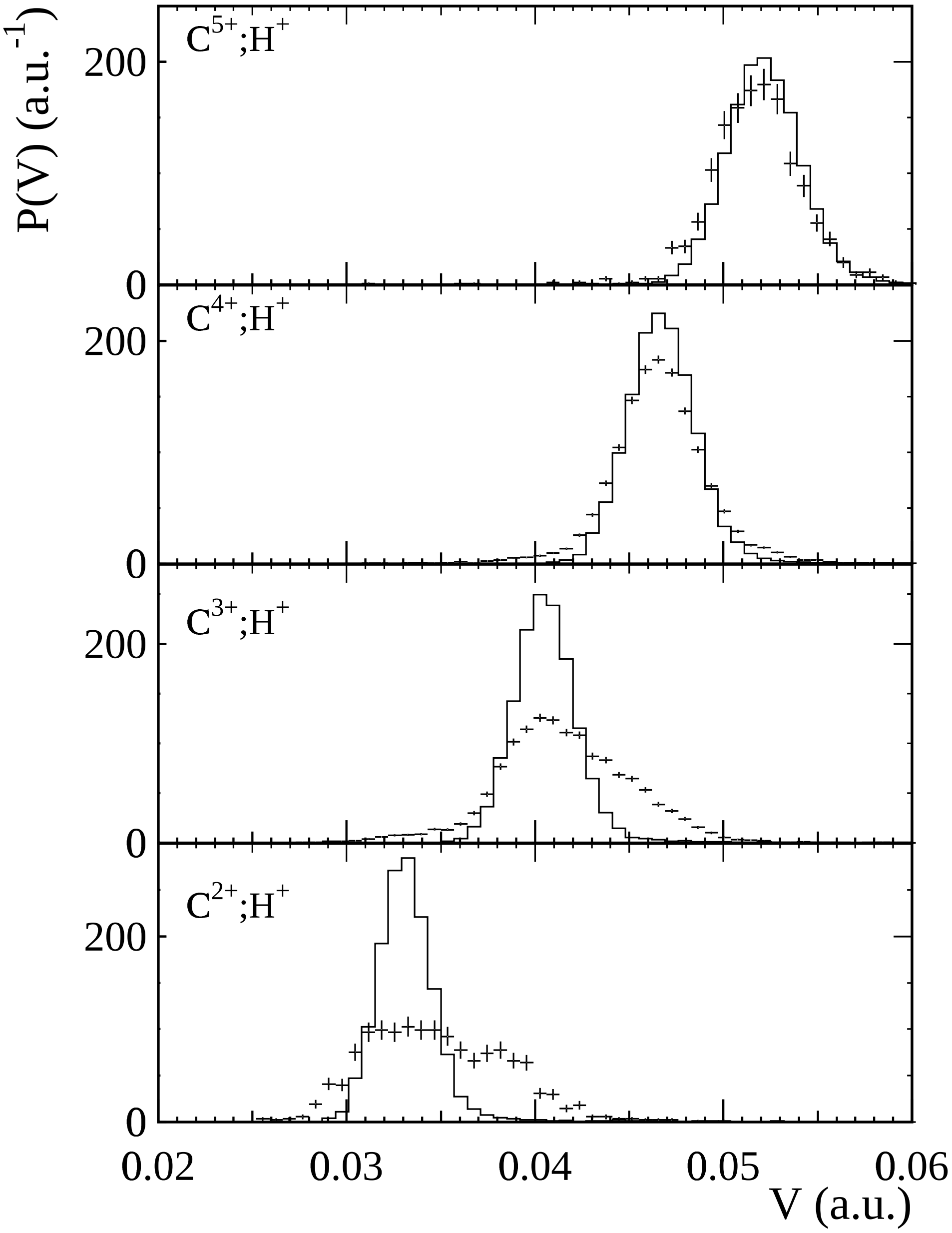

**Fig. 5.20:** *Comparison of the measurements of $CH^{+} \rightarrow Cq+$ + $H^{+}$ at 6.5 MeV (thin target, storage times between 500 ms and 2 s) to the results of the CEI simulation.*

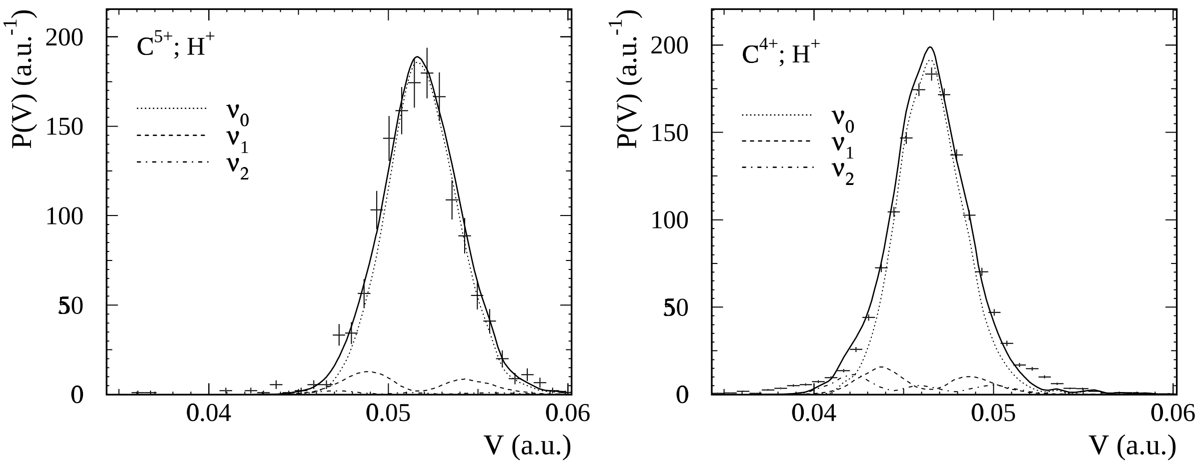

**Fig. 5.21:** *Fit of the vibrational population of the measured molecules exploding into the $C^{5+}$ + $H^+$ and $C^{4+}$ + $H^+$ charge state for storage times between 500 ms and 2 s. The fit used the first three vibrational states of the $a3\Pi$ state of $CH^+$. The fit results for both charge channels agree within the fit errors and give a population of $90 \pm 4\%$ for the vibrational ground state, $7 \pm 3\%$ for the first vibrational state and $3 \pm 3\%$ for the second vibrational state.*

because the $R$-space distributions of the vibrational states in both potentials are almost identical. The result can be seen in figure 5.21 on the left. The fit gives a good agreement with the experimental data and shows that the shift of the center as well as the larger width of the $P(V)$ distribution for the $C^{5+}$ + $H^+$ charge channel can be explained by vibrational excitation. According to the fit about $91\% \pm 3\%$ of the molecules are in the vibrational ground state about $8\% \pm 4\%$ in the first excited state so there is almost no higher vibrational excitation left. A similar picture (although the fit looks slightly worse) can be found when using the vibrational states of the $X^1\Sigma^+$ potential curve.

The same fit has been done with the $C^{4+}$ + $H^+$ charge channel (see figure 5.21 on the right) and leads within the fit errors the same vibrational population ($86 \pm 7\%$ in the vibrational ground state, $8 \pm 2\%$ in the first excited state and about $6 \pm 5\%$ in the second excited state). The fit can however not explain the tails of the distribution towards high and low relative velocities. These tails are understandable due to excitation of one of the remaining electrons. Since charge state $C^{5+}$ gets populated in the foil one can also assume that a small amount of the explosions into $C^{4+}$ and $H^+$ have one excited electron leading to explosions taking place on non Coulomb like potential curves.

The lower charge states show large deviations between the Coulomb model and the experimental distribution $P(V)$. Compared to the Coulomb model the distributions $P(V)$ are mainly shifted to larger relative velocities. However a smaller but significant tail to lower relative velocities does also exist. These effects are similar to the one already seen in the explosion of $HeH^+$ into $He^+$ and $H^+$. To be able to calculate the theoretical $V$-space distributions in these cases one has to calculate molecular potential curves of the $CH^{3+}$ and $CH^{4+}$ quasi-molecules and use them to simulate the explosion process. The tail to lower velocities can be explained by some of these electronic states inducing a binding effect between the two fragments.

Related to this it is also interesting to compare the measured $V$-space distributions at 6.5 MeV and at 4 MeV (see figure 5.22). While the distributions for the 4 MeV measurement are shifted by about 1.1% and 2.2% towards lower relative velocities for the charge states $C^{4+}$ and $C^{5+}$, compared to the 6.5 MeV measurement, they are shifted to higher relative velocities for charge states $C^{2+}$ ($\approx +4.5\%$) and $C^{3+}$ ($\approx +1.2\%$).

The $V$-space distributions measured in the dissociation channels into the charge states $C^{4+}$ and $C^{5+}$ are rather puzzling. As has been shown in the 6.5 MeV measurement the remaining electrons seem to play a minor roll in the explosion of these charge states so that the picture of different potential curves cannot explain the differences between the two measurements. The deviations between the two measurements are even larger in the lower charge state distributions. One possible explanation would be to assume that the transitions into the different dissociative potential curves that are induced by the foil occur with different probabilities at the two different energies.

The ion beam was produced by stripping in a gas jet in the terminal of the tandem. For the two beams the stripping happened at different energies. This might cause different relative populations of two electronic states. Since the $a^3\Pi$ state has a lifetime of about 7 seconds the relative population of the two states should not change much over the two seconds measurement period. Due to the fact that $CH^+$ could only be measured at short storage times it was unfortunately impossible to measure fully relaxed molecules. This would have been needed to be able to exclude influences of the vibrational and electronic excitation on the measured $V$-space distributions. Assuming vibrational and electronic excitation in the molecular beam most of the deviations seen for the dissociation into $C^{4+}$ and $H^+$ can be explained. This is however not not possible for the $C^{5+}$ channel where the center of the distribution $P(V)$ deviates by 2.2% from the measurement at 6.5 MeV and by about 3% from the simulated explosion of the $CH^+$ ground state.

Other possible effects leading to such a disagreement could be a wrong calibration of the pixel to millimeter ratio and of the beam velocity. The pixel to millimeter ratio has been checked on the measured data itself by correlating the camera clusters on each detector with the wires hit in coincidence. It is correct to about 0.4% (see section 4.6) and should show up in the same way in the 6.5 and 4 MeV measurements. The beam velocity was measured using a Schottky pickup in the storage ring TSR and is accurate to less than 0.4%. As for the 6.5 MeV measurement,

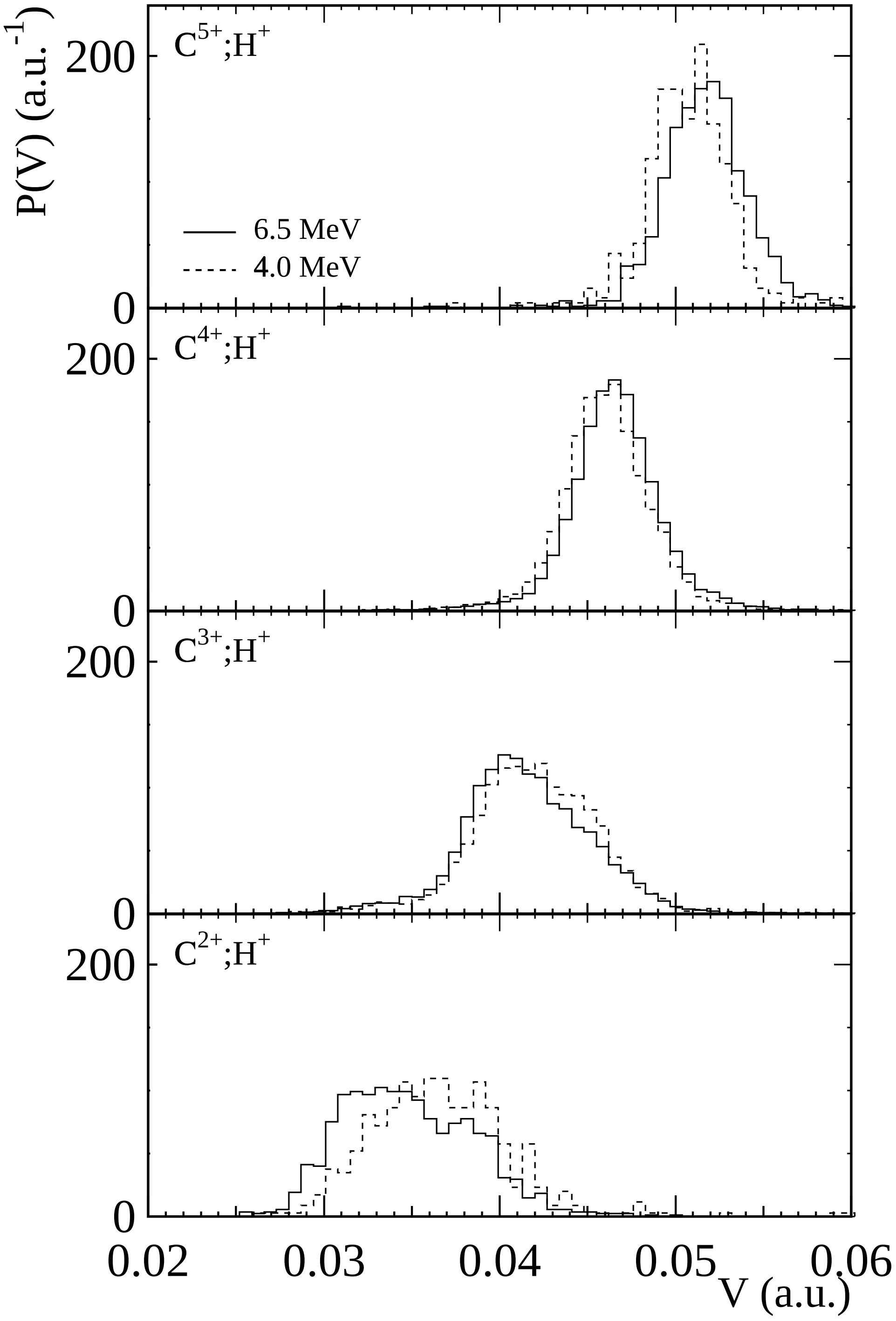

**Fig. 5.22:** *Comparison of the Coulomb explosion of* $CH^+$ *into* $C^{q+} + H^+$ *at 6.5 and 4 MeV.*

shielding effects inside the target foil can be excluded.

The $H^+$ cone of the explosion of $CH^+$ into $C^{5+}$ and $H^+$ has a diameter of about 41 mm on the detector and is thus the only case where regions in the round detector with non constant detection efficiencies are used (see section 4.4). A simulation taking into account these detection efficiencies was performed but changed the average relative velocity between the fragments only by about 0.5%.

It is still unclear which effect could cause the observed $V$-space distribution for the explosion into $C^{5+}$ and $H^+$. None of the above mentioned effects alone can be responsible for the measured discrepancy. Adding up all the above mentioned effects the discrepancy between theory and experiment can be reduced but does not vanish.

# 6. Conclusions and Outlook

This thesis has presented Coulomb explosion imaging experiments performed with the CEI setup at the heavy-ion storage Ring TSR at the Max-Planck-Institut für Kernphysik in Heidelberg. Three different molecular ions were measured and analyzed: $HeH^+$, $LiH^+$ and $CH^+$. The focus of this work was to examine the interaction potential driving the explosion process of these molecules. This was possible because the structural parameters of all three molecules are well known theoretically and for $HeH^+$ and $CH^+$ detailed experimental data is available. The results can be summarized as follows:

- The CEI measurements of $HeH^+$ and $LiH^+$ into naked fragments ($He^{2+}$, $Li^{3+}$ and $H^+$) agree very well with theoretical calculations of the molecules ground potential curve and assuming an explosion on Coulomb trajectories similar to the results obtained for $HD^+$ (see ref. [14]). The $HeH^+$ ions measured for storage times longer than 100 ms are observed to have relaxed to the vibrational ground state in agreement with findings from other experiments. $LiH^+$ was, to the best of our knowledge, for the first time studied experimentally. In this case some vibrational excitation remains and the molecular ions are not in thermal equilibrium with the surrounding storage ring. This is in agreement with the calculated lifetimes for the $LiH^+$ vibrational states.

- The explosion of $HeH^+$ into $He^+$ and $H^+$ shows a large deviation from the simulation using a simple Coulomb explosion picture. Apart from a peak at the relative velocity expected from the simulation the measured distribution shows a large tail to higher relative velocities. As the explosion into naked ions agrees with the simulation, this shows that the approach of a Coulomb explosion of two point-like particles is to simplistic to be able to describe the physics involved in this dissociation channel.

- Two models were used to explain the explosion process of $HeH^+$ into $He^+$ and $H^+$. A simple extension of the Coulomb model assumed that the electron is tied to the Helium ion and the electron wave function is not distorted by the proton. The electron then resides in a (hydrogen-like) bound state of the Helium. Under this assumption the potential between the Helium ion and the proton can be calculated analytically. Assuming some of the electrons are bound in an excited state the model agrees qualitatively with the measurement.

The second model used the dissociative potential curves obtained by a full quantum mechanical calculation of the dissociative potential curves of the $HeH^{++}$ pseudo-molecule. Using this model agreement between experiment and theory could be obtained and transition probabilities into the different dissociative states of the $HeH^{++}$ pseudo-molecule could be extracted.

- Similar features as in the $HeH^+ \rightarrow He^+ + H^+$ explosion were observed in the dissociation of $LiH^+$ into $Li^+/Li^{2+}$ and $H^+$. The dissociation into $Li^{2+}$ and $H^+$ the Coulomb model still agrees quite well with the experimental data but a tail at higher relative velocities can be observed in the measurement. This tail gets even larger for the $Li^+ + H^+$ dissociation channel. The tails are smaller than for $HeH^+$ due to the larger bond length of the $LiH^+$ molecule which reduces possible influences of the remaining electrons.

- The measurement of $CH^+$ showed similar effects as $HeH^+$ and $LiH^+$ for the low charge states ($C^{2+}$ and $C^{3+}$). One difference in the $V$-space distributions of these channels is that they also show tails to smaller relative velocities which might be due to binding effects of the electrons remaining in the system.

- The measurement of $CH^+$ did also show that for high charge states (in this case the explosion into $C^{4+}/C^{5+}$ and $H^+$) the measured data did not deviate much from the simulation. Deviations were of the order of a few percent at most and give an estimate on the accuracy of estimations that can be expected when extracting bond lengths from measured distributions.

- The measurement of the explosion of $CH^+$ into $C^{5+}$ and $H^+$ at 4 MeV showed a $V$-space distribution where the mean relative velocity between the fragments deviates by about three percent from the theoretical expectation and by more than 2% from the data measured at 6.5 MeV. It is still unclear where this deviation comes from and further investigations will be needed to resolve this.

The measurements of $HeH^+$, $LiH^+$ and $CH^+$ showed that a model using simple point like ions and an explosion on Coulomb trajectories is in many cases insufficient to explain the measured distributions in $V$-space. This implies that for low charge states, when the wave functions of the remaining electrons are not localized at one of the fragments, Coulomb explosion imaging cannot be used easily to measure bond-length distributions. Detailed calculations of the dissociative potentials driving the explosion process will be needed to be able to compare the measured $V$-space distributions for these charge states to theoretical data. Further study of the dissociation processes into low charge states and comparison to theoretical calculations might give further insight into the processes happening inside and directly after the foil.

The measurements showed that the strength of the wake effect depends on the target thickness and the velocity of the ion beam. A thicker target or a lower beam velocity leads to stronger wake effects. The exact influence of the wake fields onto the explosion process is still an open question that will need further investigations.

However it seems to be possible to use dissociations into higher charge states to extract within certain errors structural parameters from the measured $V$-space distributions. For this the discrepancy between theory and measurement in the $CH^+$ explosion into $C^{5+}$ and $H^+$ at 4 MeV has to be resolved. A measurement of $CH^+$ in the electronic and vibrational ground state could help resolving this issue. This can be achieved under regular storage ring conditions where the lifetime of the $CH^+$ beam is of the order of 10 s [55].

Measurements of bond angles are often quite insensitive to the exact shape of the dissociation potentials as was already shown in [14]. This often makes measurements of bond angles possible even without knowing the exact shape of the dissociative potential.

Using the new preamplifiers build up recently for the Coulomb explosion experiments better measurements of larger molecules where more than one particle hits the same MCP will become possible and might lead to various new and exciting measurements. New measurements on $H_3^+$ and $CH_2^+$ are already planned and will hopefully resolve the remaining discrepancies seen in older measurements of these molecules. These new preamplifiers will also help to distinguish between influences on the measured $V$-space distribution due to detector properties and effects in the target foil. This might lead to a better understanding of wake effects happening in the target foil.

The above experiments show that Coulomb explosion imaging experiments at the TSR do not only offer an opportunity to continue studying spatial structures of molecules but might also lead to new results concerning the interaction of fast ions with matter.

# References

[1] G. Herzberg, *Molecular spectra and molecular structure*, Van Nostrand Reinhold, 1950.

[2] Z. Vager, R. Naaman and E. .P. Kanter, *Coulomb explosion imaging of small molecules*, Science **244**, 426 (1989)

[3] A. Baer, m. Grieser, L. Knoll, J. Levin, R. Repnow, D. Schwalm, Z. Vager, R. Wester, A. Wolf and D. Zajfman, Ground state of $CH_2^+$: Experimental aspects and theoretical implications, Phys. Rev. A **59**, 1865 (1999)

[4] J. Levin, H. Feldman, A. Baer, D. Ben-Hamu, O. Heber, D. Zajfman and Z. Vager, *Study of unimolecular reactions by Coulomb Explosion Imaging: The nondecaying Vinylidene*, Phys. Rev. Lett. **81**, 3347 (1998)

[5] H. Stapelfeld, E. Constant, H. Sakai and P. B. Corkum, *Time resolved Coulomb Explosion Imaging: A method to measure structure and dynamics of molecular nuclear wave packets*, Phys. Rev. A, **58**, 426 (1998)

[6] R. Dörner, H. Bräuning, O. Jagutzki, V. Mergel, M. Achler, R. Moshammer, J. M. Feagin, T. Osipov, A. Bräuning-Demian, L. Spielberger, J. H. McGuire, M. H. Prior, N. Berrah, J. D. Bozek, C. L. Cocke, H. Schmidt-Böcking, *Double photoionization of spatially aligned* $D_2$, Phys. Rev. Lett. **81**, 5776 (1997)

[7] U. Werner, J. Becker, T. Farr, H. O. Lutz, *How molecules and clusters explode*, Nucl. Instrum. Methods B **124**, 298 (1997)

[8] T. Graber, D. Zajfman, E. P. Kanter, R. Naaman, Z. Vager and B. J. Zabransky, *A Source for cold molecular ions for Coulomb Explosion Imaging*, Rev. Sci. Instrum. **63**, 3569 (1992)

[9] D. Habs, W. Baumann, J. Berger, P. Blatt, A. Faulstich, P. Krause, G. Kilgus, R. Neumann, W. Petrich, R. Stockstad, D. Schwalm, E. Szmola, K. Welti, A. Wolf, S. Zwickler, E. Jaeschke, D. Krämer, G. Bisoffi, M. Blum, A. Friedrich, C. Geyer, M. Grieser, H. W. Heyng, B. Holzer, R. Ihde, M. Jung, K. Matl, W. Ott, B. Povh, R. Repnow,

M. Steck, E. Steffens, D. Dutta, T. Kühl, D. Marx, S. Schröder, M. Gerhard, R. Grieser, G. Huber, R. Klein, M. Krieg, N. Schmidt, R. Schuch, J. F. Babb, L. Spruch and A. Noda, *First experiments with the Heidelberg Test Storage Ring TSR*, Nucl. Instrum. Methods B **43**, 390 (1989)

[10] Z. Amitay, D. Zajfman, P. Forck, U. Hechtfischer, B. Seidel, M. Grieser, D. Habs, R. Repnow, D. Schwalm and A. Wolf, Dissociative recombination of $CH^+$: Cross section and final states Phys. Rev. A **54**, 4032 (1996)

[11] J. Semaniak, S. Rosen, G. Sundstrom, C. Stromholm, S. Datz, I. Danared, M. af Ugglas, M. Larsson, W. J. van der Zande, Z. Amitay, U. Hechtfischer, M. Grieser, R. Repnow, M. Schmidt, D. Schwalm, R. Wester, A. Wolf, D. Zajfman *Product-state distributions in the dissociative recombination of* $^3HeD^+$ *and* $^4HeH^+$ Phys. Rev. A, **54**, R4617 (1996)

[12] Z. Amitay, A. Baer, M. Dahan, L. Knoll, M. Lange, J. Levin, I. F. Schneider, D. Schwalm, A. Suzor-Weiner, Z. Vager, R. Wester, A. Wolf and D. Zajfman, *Dissociative Recombination of HD+ in Selected Vibrational Quantum States*, Science **281**, 75 (1998)

[13] R. Wester, F. Albrecht, M. Grieser, L. Knoll, R. Repnow, D. Schwalm, A. Wolf, A. Baer, J. Levin, Z. Vager and D. Zajfman, *Coulomb explosion imaging at the heavy ion storage ring TSR*, Nucl. Instrum. Methods A **413**, 379 (1998)

[14] R. Wester, *Spatial structure of stored molecular ions by Coulomb explosion imaging*, Dissertation, Universität Heidelberg (1999)

[15] M. J. Gaillard, D. S. Gemmell, G. Goldring, I. Levine, W. J. Pietsch, J. C. Poizat, A. J. Ratkowski, J. Remillieux and Z. Vager, *Experimental deterimination of the structure of* $H_3^+$, Phys. Rev. A **17**, 1797 (1978)

[16] A. Balkacem, E. P. Kanther, R. E. Mitchell, Z. Vager and B. J. Zabransky, *Measurement of the Ultrashort Bond Length in* $He_2^+$, Phys. Rev. Lett. **63**, 2555 (1989)

[17] Z. Vager, D. Zajfman, T. graber and E. P. Kanther, *Experimental evidence for anomalous nuclear delocalization in* $C_2H_3^+$, Phys. Rev. Lett. **71**, 4193 (1993)

[18] D. Kella and Z. Vager, *A detailed study of conformations in the ground state of* $CH_4^+$, J. Chem. Phys. **102**, 8424 (1995)

[19] Z. Amitay, A. Baer, M. Dahan, J. Levin, Z. Vager, D. Zajfman, L. Knoll, M. Lange, D. Schwalm, R. Wester, A. Wolf, I. F. Schneider and A. Suzor-Weiner Phys. Rev. A **60**, 3769-3785 (1999)

[20] H. Kreckel, *Coulomb explosion imaging von* $H_3^+$ Diplomarbeit, Universität Heidelberg (2000)

[21] E. P. Kanther, *Interaction of fast (MeV) Molecular Ions with Matter*, Comm. At. Mol. Phys. **11**, 63 (1981)

[22] D. S. Gemmell, *Collisional effects in the passage of fast molecular ions through thin foils*, Mucl. Instrum. Methods **194**, 255 (1982)

[23] I. Plesser, *The interpretation of molecular ion dissociation experiments*, Nucl. Instrum. Methods **194**, 269 (1982)

[24] D. Zajfman, G. Both, E. P. Kanter, Z. Vager, *Multiple scattering of MeV atomic and moleular ions traversing ultrathin films*, Phys. Rev. A, **41**, 2482 (1990)

[25] D. Zajfman, T. Graber, E. P. Kanter, Z. Vager, *Influence of multiple scattering on the Coulomb explosion imaging of fast molecules* Phys. Rev. A, **46**, 194 (1992)

[26] P. Sigmund, *Scaling laws governing the multiple scattering of diatomic molecules under Coulomb explosion* Phys. Rev. A, **46**, 2596 (1992)

[27] D. S. Gemell, *Collisional effects in the passage of fast molecular ions through thin foils*, Nucl. Instrum. Methods, **194**, 269 (1982)

[28] Z. Vager, D. S. Gemell, *Polarization induced in a solid by the passage of fast charged particles*, Phys. Rev. Lett. **37**, 1352 (1976)

[29] D. Zajfman, *Coulomb explosion imaging of small molecules*, Comm. At. Mol. Phys. **29**, 369 (1994)

[30] W. Moller, G. Pospiech and G. Schrieder, Nucl. Intrum. Methods **130**, 265 (1975)

[31] A. B. Wittkower and H. D. Betz, At. Data **5**, 113 (1973)

[32] J. Levin, D. Kella and Z. Vager, *Interpretation of data in multidimensional spaces and its application to CEI*, Phys. Rev. a **53**, 1469 (1996)

[33] R. Wester, *Erste Untersuchungen zur Coulomb-Explosion kalter gespeicherter Molekülionen*, Diplomarbeit, Universität Heidelberg (1996)

[34] W. E. Brittin and W. R. Chappell, *The Wigner Distribution function and Second Quantization in Phase Space*, Rev. Mod. Phys. **34**, 620 (1962)

[35] W. Demtröder, *Laserspectroscopy*, Springer (1996)

[36] Z. Amitay, D. Zajfman, P. Forck, Phys. Rev. A **50**, 2304 (1994)

[37] A. Baer, Dissertation, in preparation.

[38] R. Wester, *private communications*

[39] W. Kolos and m. Peek, Chem. Phys., **12**, 381 (1976)

[40] J. Purder, S. Civiš and C. E. Blom, Diode Laser Spectra and Potential Energy Curve for the Molecular ion $HeH^+$, J. Mol. Spectr., **153**, 701 (1992)

[41] S. Datz and M. Larson, *Radiative Lifetimes for all Vibrational Levels in the $X^1\Sigma^+$ State of $HeH^+$ and its Relevance to Dissociative Recombination Experiments in Ion Storage Rings* Physica Scripta, **46** 343 (1992)

[42] W. Roberge and A. Dalgarno, *The formation and destruction of $HeH^+$ in astrophysical plasmas*, Astrophys. J., **255**, 489 (1982)

[43] J. M. Moorhead, R. P. Lowe, J.-P. Maillard, W. H. Wehlau and P. F. Bernath, *Search for $HeH^+$ in NGC 7027* Astrophys. J., **326**, 899 (1988)

[44] A. E. Orel, K. C. Kulander and T. N. Rescigno, *Effects of open inelastic channels in the resonant dissociative recombination of $HeH^+$*, Phys. Rev. Lett., **74**, 4807 (1995)

[45] B. K. Sarpal, J. Tennyson, L. A. Morgan, *Vibrationally resolved electron $HeH^+$ collision using the non-adiabatic R-matrix method*, J. Phys. B **24**, 1851 (1991)

[46] A. Boutalib and F. X. Gadéa, J. Chem. Phys. **97**, 1144 (1992).

[47] R. J. LeRoy, *LEVEL 6.1 – A computer program Solving the radial Schrödinger Equation for bound and quasibound levels, and Calculating various Expectation values and Matrix elements*, University of Waterloo Chemical Physics Research Report CP-555R (1996)

[48] S. Krohn, *private communications*

[49] F. A. Gianturco, P. Gori Giorgi, H. Berriche, F. X. Gadea, *Computed distributions of rotovibrational transitions in LiH ($X^1\Sigma^+$) and $LiH^+$ ($X^2\Sigma^+$)*, Astron. & Astrophys. Suppl. Ser., **117**, 377 (1996)

[50] A. Sternberg and A. Dalgarno, *Chemistry in dense photon-dominated regions*, Astrophys. Journ. **99**, 565 (1995)

[51] H. Helm, P. C. Cosby, M. M. Graff and J. T. Moseley, Phys. Rev. A **25**, 304 (1982)

[52] S. Green, P. S. Bagus, B. Liu, A. D. McLean, and m. Yoshimine Phys. Rev. A **5**, 1614 (1972); R. P. Saxon, K. Kirby and B. Liu, J. Chem. Phys. **73**, 1873 (1980); R. P. Saxon and B. Liu, J. Chem. Phys **78**, 1344 (1983); B. Levy, J. Ridard and E. Le Coarer, Chem. Phys. **92**, 295 (1985)

[53] U. Hechtfischer, private communications

[54] F. R. Ornellas and F. B. C. Machado, Journ. Chem. Phys. **84**, 1296 (1986)

[55] U. Hechtfischer, Z. Amitay, P. Forck, M. Lange, J. Linkemann, M. Schmitt, U. Schramm, D. Schwalm, R. Wester, D. Zajfman and A. Wolf, *Near-Threshhold Photodissociation of Cold $CH^+$ in a Storage Ring*, Phys. Rev. Lett., **80**, 2809 (1998)

[56] F. Albrecht, *Langsame Extraktion am Heidelberger Speicherring TSR*, Dissertation, Universität Heidelberg, 1996

[57] F. Albrecht, M. Beutelsbacher, M. Grieser, R. von Hahn, L. Knoll, R. Repnow, D. Schwalm, K. Tetzlaff and R. Wester, *Slow extraction at the Heidelberg Heavy Ion Storage Ring TSR*, Fifth European Particle Accelerator Conference (Barcelona), vol. 3, p. 2459 (1996)

[58] G. Wissler, *Untersuchungen zur langsamen Extraktion am Heidelberger Schwerionenspeicherring TSR*, Diplomarbeit, Universität Heidelberg, 1998

[59] G. Both, E. P. Kanther, Z. Vager, B. J. Zabransky and D. Zajfman, *Ultrathin foils for Coulomb explosion experiments*, Rev. Sci. Instrum. **58**, 424 (1987)

[60] V. Kh. Liechtenstein, T. M. Ivkova, E. D. olshanski, I. Feigenbaum, R. DiNardo and M. Doebeli, *Preparation and evaluation of thin diamond-like carbon foils for heavy-ion tandem accelerators and time-of-flight spectrometers*, Nucl. Instrum. Methods A **397**, 140 (1997)

[61] J. Levin, L. Knoll, M. Scheffel, D. Schwalm, R. Wester, A. Wolf, A. Baer, Z. Vager, D. Zajfman and V. Kh. Liechtenstein, *Application of ultrathin diamond-like carbon targets to Coulomb explosion imaging* , to be published

[62] D. Kella, M. Algranati, H. Feldman, O. Heber, H. Kovner, E. Malkin, E. Miklazky, R. Naaman, D. Zajfman, J. Zajfman and Z. Vager, *A system for Coulomb exlosion imaging of small molecues at te Weizmann Institute*, Nucl. Instrum. Methods A **329**, 440 (1993)

[63] M. Scheffel, *Untersuchung orts- und zeitauflösender Mehrteilchen-Detektoren mit Laserpulsen*, Diplomarbeit, Universität Heidelberg, 1999

[64] T. Jacob and S. Fritzsche, *private communications*

[65] N. Bjerre and S. R. Keiding, Phys. Rev. Lett. **56**, 1459 (1986)